

# **IDEA** League

MASTER OF SCIENCE IN APPLIED GEOPHYSICS  
RESEARCH THESIS

---

## **Quantification of acquisition uncertainties in seismic wavefield deghosting**

**Karel S. Goense**

---

August 28, 2017



# **Quantification of acquisition uncertainties in seismic wavefield deghosting**

MASTER OF SCIENCE THESIS

for the degree of Master of Science in Applied Geophysics  
by

Karel S. Goense

August 28, 2017



IDEA LEAGUE  
JOINT MASTER'S IN APPLIED GEOPHYSICS

Delft University of Technology, The Netherlands  
ETH Zürich, Switzerland  
RWTH Aachen, Germany

Dated: *August 28, 2017*

Supervisor(s):

---

Dr.ir. R.F. Hegge

---

Prof. dr.ir. C.P.A. Wapenaar

Committee Members:

---

Dr.ir. R.F. Hegge

---

Prof. dr.ir. C.P.A. Wapenaar

---

Prof. J.F. Wellmann Ph.D.



---

# Abstract

Marine seismic acquisition is troubled with several factors of noise that can deteriorate seismic data. Marine seismic data are recorded with towed streamers that acquire the desired upgoing wavefields containing information of the geology beneath. The upgoing wavefield will travel past the streamer/hydrophone to be reflected at the sea surface and propagate back down to be collected as undesired downgoing (ghost) wavefields, before propagating further downward as a surface related multiple. Because up- and downgoing wavefields interfere, these ghost wavefields generate peaks and notches in the recorded amplitude spectrum that compromises the bandwidth, reducing the resolution and the interpretability of the seismic data. Two classes of ghosts exist - source and receiver - that can be removed ('deghosting') through two main approaches; utilizing different acquisition strategies and/or computer based processing algorithms. Additional measurements may prove useful in acquiring broadband data but may be hampered by high costs and limited availability. Vast amounts of 2-D single streamer legacy data exist that can still benefit from enhanced deghosting techniques. Acquisition uncertainties, such as the unknown exact depth of sources and receivers, the unknown reflectivity of the free-surfaces, and the unknown propagation velocity of seismic waves in water, lead to an increased complexity in finding a solution to the deghosting problem. In this thesis, sensitivity analysis has shown that a variability in the propagation velocity of seismic waves in water has the greatest effect on the conventional 2D receiver deghosting result. The least sensitive parameter turned out to be the water surface reflectivity. A multitude of adaptive deghosting techniques - which optimize the parameter settings through data driven optimization - have been found in literature and are summarized to identify the shortcomings. A quantitative uncertainty analysis into these methods seems to be missing. A new adaptive deghosting method based on echo-deblending is introduced that incorporates an uncertainty analysis. Results look promising for determining receiver depths, however, the water surface reflectivities results are more challenging. Recommendations for future work to improve the method are given for future students pursuing the topic.



---

# Acknowledgements

I would like to thank Aramco and the team in Delft for their support during these six months of pursuing my thesis. First and foremost I would like to thank Rob Hegge who has been a great supervisor, knowing when to give me time to think and when to increase the pressure to get things into motion. His knowledge and experience has helped me into becoming a beginning researcher myself. I would also like to thank Hannes Kutscha for his insightful talks we had across our desks and the aid he supplied at the beginning of my thesis into re-understanding the principle concepts of geophysics. Jewoo Yoo laid the ground work for my study and even though it was a tough nut to crack his Fortran code, I was very thankful in the help he provided into understanding almost every bit of it. Roald van Borselen was able to provide clear structure to my thesis which I am very grateful for, without his help I would not have been able to deliver a sound thesis on time.

I would like to thank Prof. Kees Wapenaar for the interesting lectures he gave at the beginning of the master period. He was able to make difficult geophysical concepts easy to understand. It created a solid understanding for me and mostly increased my enthusiasm for the theoretical side of geophysics and eventually led me into doing my thesis in Delft.

Besides the researchers around me I would also like to thank my family for their support when I broke my ankle halfway through the six months, bringing me back and forth to work whenever needed and offering me all the space in the house to work on my thesis. Last but not least my girlfriend has been a great help, both in providing the space and time for me to work and be a listening ear to troubles I encountered.



---

# Table of Contents

<b>Abstract</b>	<b>v</b>
<b>Acknowledgements</b>	<b>vii</b>
<b>1 Introduction</b>	<b>1</b>
1-1 Aim of this thesis . . . . .	4
<b>2 Ghosts and methods to remove them</b>	<b>5</b>
2-1 Mathematical framework for describing ghosts and deghosting . . . . .	5
2-2 Acquisition-based deghosting . . . . .	9
2-3 Processing-based deghosting . . . . .	10
2-4 Sensitivity analysis . . . . .	11
2-5 Adaptive deghosting . . . . .	15
2-5-1 Single sensor adaptive deghosting (SSAD), Rickett et al. 2014 . . . . .	15
2-5-2 Energy minimization, Schuberth 2015 . . . . .	15
2-5-3 Adaptive windowed deghosting, Zhang et al. 2016 . . . . .	16
2-5-4 Adaptive receiver deghosting for deep-tow pressure data, Mehdi et al. 2016	16
2-5-5 Adaptive deghosting by Kurtosis maximisation, Grion et al. 2015 . . . . .	16
2-5-6 Premigration deghosting for marine streamer data using a bootstrap approach in Tau-P Domain, Wang et al. 2013 . . . . .	17
2-5-7 Hydrophone-only receiver deghosting using a variable sea surface datum, King and Poole 2015 . . . . .	17
2-6 Summary . . . . .	17
<b>3 Echo deblending</b>	<b>19</b>
3-1 The algorithm . . . . .	20
3-2 Coincidence filtering . . . . .	27

---

<b>4</b>	<b>Adaptive echo-deblending with coincidence filtering</b>	<b>31</b>
4-1	Minimizing residuals . . . . .	31
4-2	Windowing . . . . .	32
4-3	Event tracking . . . . .	34
4-4	Uncertainty analysis . . . . .	35
4-5	Test case 1: Two different receiver depths . . . . .	37
4-6	Test case 2: Two different water surface reflectivities . . . . .	39
4-7	Test case 3: Unknown water surface reflectivity and receiver depth . . . . .	40
<b>5</b>	<b>Conclusion and Recommendations</b>	<b>49</b>
	<b>Bibliography</b>	<b>51</b>
<b>A</b>	<b>Appendices</b>	<b>55</b>
A-1	The L1 and L2 norms versus Kurtosis . . . . .	55
A-2	Direct inversion-based deghosting . . . . .	56
A-2-1	1-D deghosting . . . . .	56
A-2-2	2-D deghosting . . . . .	60

---

# List of Figures

1-1	Sources of energy, now and in the future, image from [BP, 2016]. . . . .	1
1-2	Seismic surveying, image from [wik, 2010]. . . . .	3
2-1	Primary wavefield . . . . .	8
2-2	Receiver ghost . . . . .	8
2-3	Example of a primary wavefield (top) and a ghost (middle) with reverse polarity and shifted in time. Combination of the two show a loss of frequencies (bottom). . . . .	9
2-4	Different acquisition systems, figure from [Schuberth, 2015]. . . . .	10
2-5	Deghosting with wrong receiver depth ( $x_3^R = 19$ m). . . . .	12
2-6	Deghosting with wrong water surface reflectivity ( $r_c = -0.95$ ). . . . .	12
2-7	Sensitivity of result in $t - x$ on deghosting parameters. . . . .	13
2-8	Sensitivity of result in $f - k$ on deghosting parameters. . . . .	13
2-9	Sensitivity of result in $t - x$ on deghosting parameters with 10 % noise present. . . . .	14
2-10	Sensitivity of result in $f - k$ on deghosting parameters with 10 % noise present. . . . .	14
2-11	Finding delay-time using $L_1$ , $L_2$ , and Kurtosis, figure from [Zhang et al., 2016]. . . . .	16
2-12	Finding delay-time and water surface reflectivity using Kurtosis of the autocorrelation, figure from [Grion et al., 2015]. . . . .	17
3-1	Receiver ghost wavefield expressed as a mirrored receiver ghost wavefield. . . . .	19
3-2	The raw data is used as initial estimates of the primary and ghost receiver wavefields. . . . .	20
3-3	Estimate of primary wavefield at sea level obtained after forward extrapolation; the wavefield arrives later than before. . . . .	20
3-4	Estimate of ghost wavefield at sea level obtained after backward extrapolation; the wavefield arrives earlier than before. . . . .	21
3-5	Summing and halving of forward and backward extrapolated wavefields. . . . .	22
3-6	Backward extrapolation of data after thresholding. . . . .	23

3-7	Forward extrapolation of data after thresholding. . . . .	23
3-8	New estimate of the up-going primary wavefield. . . . .	24
3-9	New estimate of the ghost wavefield. . . . .	24
3-10	Residual after 1, 3, 5 and 7 iterations. . . . .	25
3-11	Behaviour of the SAR with iteration when using amplitude thresholding. . . . .	25
3-12	Loop diagram describing iterative echo-deblending. . . . .	26
3-13	Upward going wavefield after 1, 3, 5 and 7 iterations using amplitude thresholding. . . . .	27
3-14	Upward going wavefield after 1, 3, 5 and 7 iterations using coincidence filtering. . . . .	28
3-15	Behaviour of the residual with iteration when using coincidence filtering instead of amplitude thresholding. . . . .	29
4-1	SAR for range of receiver depths (18 m - 22 m in steps of 0.02 m). . . . .	32
4-2	Pyramid sliding . . . . .	33
4-3	Obtaining receiver depth, tested with $z_r = 18$ m - 22 m. . . . .	34
4-4	Obtaining water surface reflectivity, tested with $r_c = -1, -0.99, \dots, -0.7$ . . . . .	34
4-5	Standard deviation, wrong effective receiver depth ( $z_r = 18$ m). . . . .	36
4-6	Standard deviation correct effective receiver depth ( $z_r = 20$ m). . . . .	36
4-7	Standard deviation effective water surface reflectivity, tested with $r_c = -1, -0.99, \dots, -0.7$ . . . . .	37
4-8	Obtaining varied receiver depth, first event receiver depth at 22 m and second at 18 m. Window size of 51x51. . . . .	38
4-9	Standard deviation, first event receiver depth at 22 m and second at 18 m. Window size of 51x51. . . . .	38
4-10	Obtaining varied water surface reflectivities, first event water surface reflectivity at -0.9 and second at -0.95. Window size of 51x51. . . . .	39
4-11	Standard deviation, varied water surface reflectivities, first event receiver depth at -0.9 and second at -0.95. Window size of 51x51. . . . .	39
4-12	AED result, tested with receiver depths 14 m - 30 m. Window size 51x51. . . . .	40
4-13	Standard deviation of AED receiver depth result. . . . .	40
4-14	First event effective receiver depth. . . . .	41
4-15	Second event effective receiver depth. . . . .	41
4-16	1st event effective receiver depth standard deviation. . . . .	42
4-17	2nd event effective receiver depth standard deviation . . . . .	43
4-18	AED result, tested with $r_c = -1, -0.99, \dots, -0.7$ . . . . .	43
4-19	Standard deviation effective water surface reflectivities. . . . .	44
4-20	1st event effective water surface reflectivity. . . . .	45
4-21	2nd event effective water surface reflectivity. . . . .	45
4-22	1st event effective water surface reflectivity standard deviation. . . . .	46
4-23	2nd event effective water surface reflectivity standard deviation. . . . .	47
A-1	Example of low (LHS figure), high (middle figure) and middle (RHS figure) kurtosis. Figure from [Liang et al., 2008]. . . . .	56

---

A-2	Frequency spectrum of ghost operator. . . . .	57
A-3	Frequency spectrum of deghosting operator. . . . .	58
A-4	Comparing change in deghosting operator as parameters are varied. . . . .	58
A-5	Time (LHS) and frequency (RHS) amplitude plots of primary (top) wavefield, primary + ghost (second row), deghosted result (third row) and the difference in primary and deghosted (bottom). . . . .	59
A-6	Deghosted result with a stabilization factor $\lambda = 0.1$ . . . . .	60
A-7	Wave propagating at an angle. . . . .	60
A-8	Frequency spectrum of 2-D deghosting operator. . . . .	61
A-9	2D deterministic deghosting result. Left column indicates $f - k$ spectra of data with ghost (top LHS) and deghosted (bottom LHS). Right column indicates zoomed in $t - x$ plots of data with ghost (top RHS) and deghosted (bottom RHS). . . . .	62
A-10	The $f - k$ spectra (LHS) and $t - x$ plot (RHS) of 2D primary upgoing wavefield. . . . .	62
A-11	2D deghosted result with $\lambda = 0.1$ . . . . .	63
A-12	Sensitivity result when varying deghosting parameters, t-x domain. . . . .	64



---

# List of Tables

2-1	Range of values of receiver depth, water surface reflectivity and velocity used to compare with model. . . . .	13
A-1	Different range of values of receiver depth, reflection coefficient and velocity used to compare with model. . . . .	63



---

# Chapter 1

---

## Introduction

Over the past two centuries the world has seen a tremendous increase in energy use. The International Energy Agency (IEA) recently predicted the demand for energy to increase further, mainly due to rising economies in third world countries [IEA, 2016]. The IEA predicts that global natural gas demand is to increase by more than 50 percent by 2040 and global oil demand to increase from 90 million barrels per day (mbpd) in 2013 to 104 mbpd in 2040. Despite the rise of renewable energy as alternative source of energy, it is clear that fossil fuels will remain to play a predominant role in the energy mix for many years to come (see Figure 1-1).

Primary energy consumption by fuel

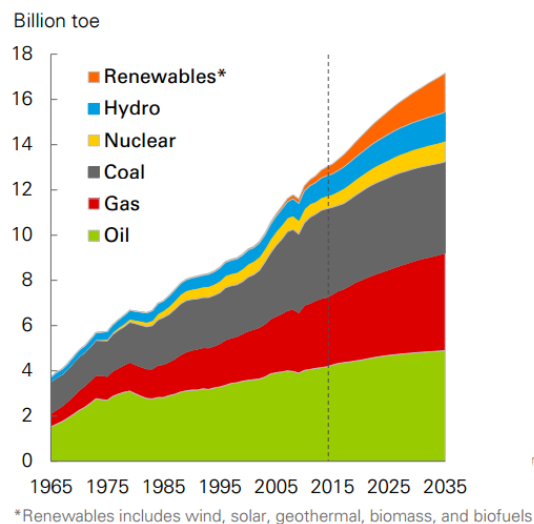


Figure 1-1: Sources of energy, now and in the future, image from [BP, 2016].

The rising demand for fossil fuels poses a significant challenge for the oil & gas industry. On the one hand, remaining oil & gas reservoirs are becoming increasingly more difficult to

find due to complexity at the reservoirs. The current spatial and temporal resolutions are found to be no longer sufficient to find smaller and more complex oil & gas accumulations. Furthermore, because of lower oil prices, oil and gas companies are spending less resources on finding new reservoirs. Also, their appetite for investing resources in R&D is under pressure. On the positive side, recent technological advances and innovations in oil & gas exploration have made it possible to counter these challenges. Oil and gas companies have been able to increase their output by embracing innovation solutions at production level (by implementing mechanical or chemical techniques that improve the production of liquids in existing oil and gas fields) and at exploration level, by generating high-resolution images of the subsurface that, eventually, contribute to drilling wells more successfully.

Seismic images are obtained by conducting geophysical experiments and processing the acquired data. Using controlled sources, waves are sent down into the subsurface and, after propagation through the subsurface, recorded as a function of space and time. Rocks in the subsurface each have a unique set of material properties such as density, compressibility, electrical resistance. As a result, rocks react differently to the waves that they are exposed to. For example, rocks that contain fluids with a higher electrical resistance (e.g. oil) will not allow electric signals to pass through them easily compared to rocks filled with water. Seismic signals encounter a lower resistance when propagating through materials with greater density. Based on these characteristics, it is possible to generate images of the subsurface, as discontinuities in rock properties are embedded in the received signals.

In seismic data acquisition, seismic sources generate waves that propagate downwards into the subsurface. The seismic waves are reflected at subsurface reflectors where the material properties are discontinuous. A complementary portion of the seismic wave is being transmitted at the seismic reflector. Reflected seismic waves move upwards and may reflect again against an internal reflector. After reflection and transmission of the waves in the subsurface, a portion of the emitted wavefield is eventually recorded with a set of receivers. For each source and receiver pair, the recorded signals are digitized and stored as a time series of amplitudes representing the seismic waves. These signals are then processed through the utilization of a series of processing steps to re-organize, clean-up and focus the recorded signals, after which an image of the subsurface is obtained. A geologist will then interpret the image and create a geological map that can be used to determine where to drill, or not to drill.

In marine seismic data acquisition, seismic vessels equipped with a number of airguns are utilized to generate seismic pressure wavefields. Seismic vessels may also carry a number of streamers that contain a set of hydrophones that record the seismic signal at equal distances along the streamer spread (fig. 1-2).

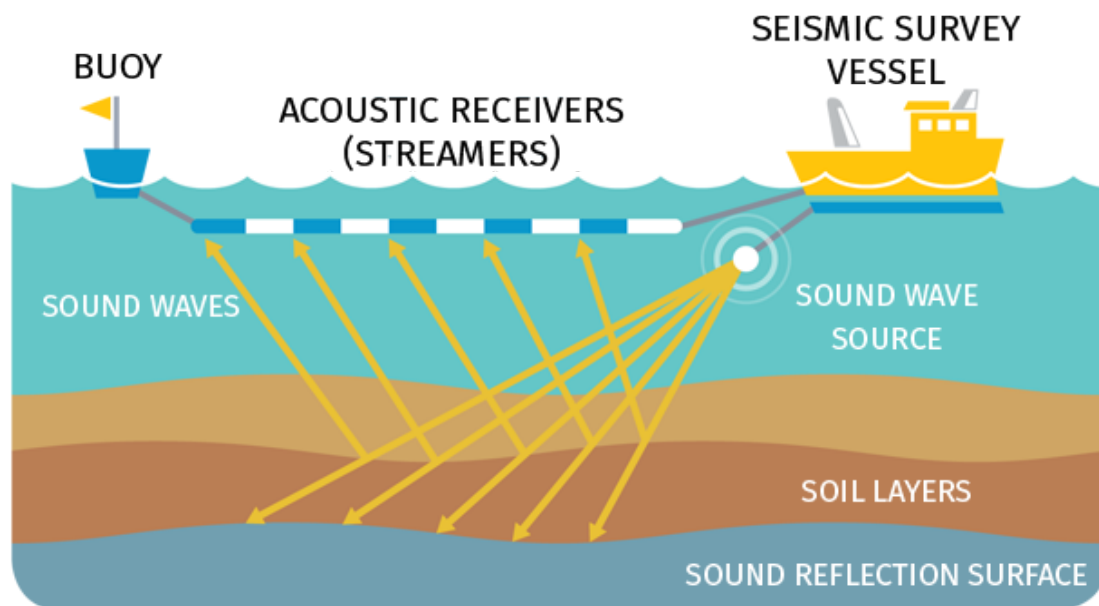


**Figure 1-2:** Seismic surveying, image from [wik, 2010].

After data acquisition, seismic data processing is utilized to create the seismic images. One of the first steps in data processing is to remove the recorded noise from the data. There are two main forms of noise: experimental and erratic. Experimental noise occurs due to imperfections occurring during acquisition, such as defect and/or missing sources or receivers. Examples of erratic noise are wind motion / wave action causing receiver cable vibrations, instrumental noise and mammal activity causing background vibrations. Another source of erratic noise is the sea surface creating seismic multiples and seismic ghost events. Surface-related multiples are events that have travelled through the water layer more than once as they have been reflected by the free-surface. Ghost events are also created by the free-surface. Each upgoing wavefield that is recorded by the hydrophones is followed by an event that has propagated further to the free surface, where it is reflected back into the water layer before it is recorded at the hydrophones. In other words, each seismic event is recorded twice: first as an up-going wavefield that has been reflected by the subsurface, and then as a ghost, which is the down-going field that has been reflected by the free-surface. Similarly, the seismic energy emitted by the seismic sources consists of two constituents: one component propagates directly downwards into the subsurface, the second component propagates upwards to the free-surface before it is reflected off the free-surface again to propagate as a down-going wavefield. As a result, interference patterns between up- and down-going wavefields are present in the recorded data, causing peaks and notches in the amplitude spectrum of the recorded data. This compromises the bandwidth, resolution and the interpretability of the data. It is therefore desirable to remove the ghost events from the data.

Removal of ghost events, also known as deghosting, is a longstanding problem in marine seismic exploration. The complexity of the problem arises from the many acquisition uncertainties that are encountered during data acquisition, such as the unknown exact location and depth of the sources and receivers, the unknown reflectivity of the free-surface that creates

the ghosts, the unknown propagation velocity of the seismic waves in water (that depends on temperature and salinity). These uncertainties may lead to erroneous results after processing.

## **1-1 Aim of this thesis**

This thesis focusses on the deghosting of marine seismic data, aiming to understand and improve deghosting in case of acquisition uncertainties due to unknown reflectivity at the free-surface, and unknown source and receiver depths. In chapter two, seismic ghost events are described with the aid of the wave-equation. The impact of acquisition uncertainties on ghost wavefields is investigated. Several deghosting methods that have been proposed in the literature are reviewed, including methods that aim to address acquisition uncertainties through adaptive deghosting. Chapter three discusses Echo-deblending, a relatively new approach that describes ghosts as events generated by secondary or blended sources. Separation of these events through non-linear filtering of extrapolated results accomplishes source deghosting. Due to acoustic reciprocity the same principles will hold in receiver deblending as a case of receiver deghosting. Chapter four discusses the new development presented in this thesis, a method to determine and quantify the unknown water surface reflectivity and source and receivers depths from the seismic data. Results from synthetic experiments are presented, showing the robustness of the method developed. Finally in chapter five, conclusions are drawn and recommendations for further development are provided.

# Ghosts and methods to remove them

The presence of ghost events hamper the quality of the data. Due to the presence of the free-surface, complex interference patterns between up- and down-going wavefields are present in the recorded data, causing peaks and notches in the amplitude spectrum of the recorded data. This compromises the bandwidth, resolution and the interpretability of the data, and hence it is desirable to remove the ghost events from the data, a process referred to as deghosting. The phenomenon of ghost events present in marine seismic data can be well described using the acoustic wave equations. In the following sections, a mathematical framework is presented that can be used to describe ghosts, and methods to remove the ghosts from the data, i.e. deghosting.

## 2-1 Mathematical framework for describing ghosts and deghosting

Many authors have described the physics and mathematics behind ghosts and the concept of deghosting, such as [Wapenaar and Berkhout, 1989] and [Fokkema and van den Berg, 1993]. The framework described below follows closely the work by the latter, [Fokkema and van den Berg, 1993]. The seismic quantities that describe the acoustic waves, depend on position and on time. To register a position a Cartesian reference frame is used with three base vectors  $\{i_1, i_2, i_3\}$  that are mutually perpendicularly oriented and are of unit length each. The property that each base vector specifies geometrically a length and an orientation, makes it a vectorial quantity, or a vector.  $\{x_1, x_2, x_3\}$  denotes the three numbers needed to specify a position, the vectorial position of the observer  $\mathbf{x}$  is the linear combination

$$\mathbf{x} = x_1 \mathbf{i}_1 + x_2 \mathbf{i}_2 + x_3 \mathbf{i}_3. \quad (2-1)$$

To register the time we consider an interval  $\mathbb{T} = \{t \in \mathbb{R}; t > t_0\}$ , where  $t_0$  is the switching time of the seismic sources. In signal processing one is usually interested in the frequency representation/spectrum of a set of signals. Frequency in this case, is the number of occurrences

of a repeating signal per unit time ( $f = \frac{1}{t}$ ), also called temporal frequency. To obtain the frequency spectrum  $\hat{\psi}(\mathbf{x}, f)$  of a space-time based signal  $\psi(\mathbf{x}, t)$ , a temporal Fourier transform of the signal is carried out:

$$\hat{\psi}(\mathbf{x}, f) = \int_{-\infty}^{\infty} \psi(\mathbf{x}, t) e^{-2\pi j f t} dt \quad (2-2)$$

The corresponding backward temporal Fourier transformation for a real-valued signal is defined as:

$$\hat{\psi}(\mathbf{x}, t) = 2Re\left(\int_0^{\infty} \hat{\psi}(\mathbf{x}, f) e^{2\pi j f t} df\right) \quad (2-3)$$

The integral is taken from 0 to infinity due to redundant information in the negative frequencies and its Hermitian symmetry around the frequency axis.

In these equations,  $t$  is time,  $j = \sqrt{-1}$  is the imaginary unit, and  $f$  is the temporal Fourier frequency parameter. The absolute values of the complex numbers obtained after the forward Fourier transform represent the amplitudes of the corresponding frequencies in the original function. The result of taking the absolute values of a Fourier transformed dataset can be plotted in what is called an amplitude/frequency spectrum. Another attribute that can be obtained from the result of a Fourier transform is the phase of the signal. The phase of a signal represents the position of a point in time on a waveform cycle, where one cycle contains  $360^\circ$  or expressed in radians as  $2\pi$ . Changing the phase of a signal will cause the signal to move forward or backward in time.

The  $x_3$ -coordinate is commonly assigned to the vertical depth position. Subsequently,  $x_1$  and  $x_2$  represent the horizontal positions. If a wavefield is assigned as  $u = u(\mathbf{x}, t)$  and  $\hat{u} = \hat{u}(\mathbf{x}, f)$  denotes its temporal Fourier transform, then the spatial Fourier transform pair  $\{F, F^{-1}\}$  of function  $\hat{u}$  is then defined as

$$F\{\hat{u}(x_1, x_2, x_3, \omega)\} = U(p_1, p_2, x_3, \omega) = \int_{(x_1, x_2) \in R^2} \hat{u}(x_1, x_2, x_3, \omega) e^{j\omega p_1 x_1 + j\omega p_2 x_2} dA, \quad (2-4)$$

$$F^{-1}\{U(p_1, p_2, x_3, \omega)\} = \hat{u}(x_1, x_2, x_3, \omega) = \left(\frac{\omega}{2\pi}\right)^2 \int_{(p_1, p_2) \in R^2} U(p_1, p_2, x_3, \omega) e^{-j\omega p_1 x_1 - j\omega p_2 x_2} dA, \quad (2-5)$$

in which  $\{p_1, p_2\}$  are the horizontal components of the slowness  $\mathbf{p}$ , defined in terms of its Cartesian components

$$\mathbf{p} = p_1 i_1 + p_2 i_2 + p_3 i_3. \quad (2-6)$$

Note that  $\omega \mathbf{p} = \mathbf{k}$  with angular wavenumber  $\mathbf{k} = \frac{\omega}{c} \mathbf{k}$ ,  $\mathbf{k} = k_1 i_1 + k_2 i_2 + k_3 i_3$ ,  $\omega = 2\pi f$ , and  $c$  the propagation velocity of acoustic waves inside a medium. The acoustic wave equations are representative for the action of mechanical forces and the influence of inertia during the acoustic wave motion as well as of the deformation that take place during this wave motion [Fokkema and van den Berg, 1993]. In the time-space domain, the acoustic wave equations have the form

$$\partial_n p + \rho \partial_t v_n = f_n, \quad (2-7)$$

$$\partial_n v_n + \kappa \partial_t p = q, \quad (2-8)$$

where the boundary conditions are such that pressure  $p$  and the particle velocity in the direction perpendicular across interface  $S$ ,  $\nu_n v_n$ , are continuous across  $S$  [Fokkema and van den Berg, 1993], where any interface  $S$  represents a discontinuous change in medium parameters. Note that  $p$  is the acoustic pressure in (Pa),  $f_n$  is the volume source density of volume force ( $N/m^3$ ),  $v_n$  represents the particle velocity (m/s),  $q$  volume source density of injection rate ( $s^{-1}$ ), and  $\partial_n$  represents differentiation with respect to spatial coordinates  $x_n$ ,  $n = 1, 2, 3$ . The medium is represented by the volume density of mass,  $\rho$ , ( $kg/m^3$ ), and the compressibility,  $\kappa$ , ( $Pa^{-1}$ ).

Using reciprocity theorems [Fokkema and van den Berg, 1993], it is now possible to decompose the total pressure wavefield in the half-space  $0 < x_3 < \infty$  (bounded by the plane water surface at depth  $x_3 = 0$ ) into an incident wavefield and a scattered wavefield (in the temporal Fourier-transform domain)

$$\hat{p}(\mathbf{x}; \mathbf{x}^S) = \hat{p}^{inc}(\mathbf{x}; \mathbf{x}^S) + \hat{p}^{sct}(\mathbf{x}; \mathbf{x}^S). \quad (2-9)$$

where the incident wavefield is initiated by monopole sources of volume injection type, located at  $x^S$  and at the mirror location of  $\{x_1^S, x_2^S, -x_3^S\}$ , generating the source ghost.

When only the scattered waves are considered, the following wavefield decomposition can be arrived at

$$\hat{p}^{sct}(x_1, x_2, x_3^R; \mathbf{x}^S) = \hat{p}^{down}(x_1, x_2, x_3^R; \mathbf{x}^S) + \hat{p}^{up}(x_1, x_2, x_3^R; \mathbf{x}^S), \quad (2-10)$$

in which  $\hat{p}^{up}$  can be formulated in the slowness domain as:

$$P^{up}(p_1, p_2, x_3; \mathbf{x}^S) = \frac{e^{j\omega\Gamma x_3}}{2\sinh(j\omega\Gamma x_3^R)} P^{sct}(p_1, p_2, x_3^R; \mathbf{x}^S), \quad (2-11)$$

and

$$\Gamma = \sqrt{\frac{1}{c^2} - p_1^2 - p_2^2}, \quad Re(\Gamma) > 0. \quad (2-12)$$

This equation suggests that the scattered wavefield can be decomposed into up- and down-going wavefields in a straightforward way. It is important to realize that the denominator on the right-hand side effectively collapses the responses from monopole point receivers located at depths  $x_3^R$  and  $-x_3^R$  to a single measurement at depth level  $x_3^R = 0$ , after which the  $e^{j\omega\Gamma x_3}$  operator shifts the recording back to any desired depth level  $x_3$ .

When describing ghosts and deghosting processes, wavefield extrapolation operators are commonly used. The forward extrapolation operator  $W^-(x_3^0, x_3^R)$  (minus sign indicates upward extrapolation, forward in time) is applied to the real receiver wavefield  $P^{up}(x_3^R; x_3^0)$  to get the real receiver wavefield at the sea level  $P^{up}(x_3^0; x_3^0)$ :

$$P^{up}(x_3^0; x_3^0) = W^-(x_3^0, x_3^R) P^{up}(x_3^R; x_3^0). \quad (2-13)$$

Application of this operator brings the real receiver from  $x_3^R$  m to  $x_3^0$  m. The forward extrapolation operator ( $W^-$ ) can be expressed as the one way wavefield extrapolator  $e^{j\omega\Gamma\Delta x_3}$ , with  $\Delta x_3 = x_3^R - x_3^0$ . The corresponding backward extrapolation operator  $F^+(-x_3^R, x_3^0)$  can be described as the conjugate of the forward operator and is composed of the term  $e^{-j\omega\Gamma\Delta x_3}$ . Application of this operator to a downward propagation field, as in:

$$P^{down}(x_3^0; x_3^0) = F^+(x_3^0, -x_3^R)P^{down}(-x_3^R; x_3^0) \quad (2-14)$$

brings the ghost receiver from  $-x_3^R$  m to  $x_3^0$  m.

The upgoing signal transmitted by the sea floor may be called the primary upgoing wavefield and it is recorded directly at the hydrophone at depth level  $x_3^R$  (fig. 2-1). The wavefield that continues to propagate upwards, which becomes a downgoing wavefield after reflection at the free-surface may be called the secondary wavefield. Alternatively, it can be considered to be recorded at mirror depth level  $-x_3^R$ . This signal is referred to as a receiver ghost (fig. 2-2).

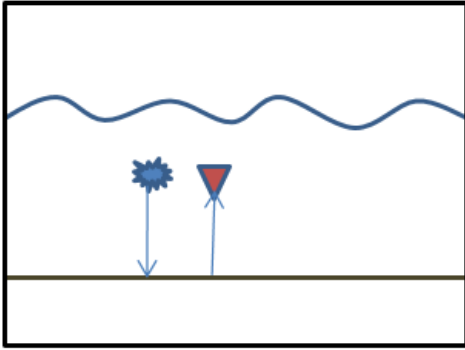


Figure 2-1: Primary wavefield

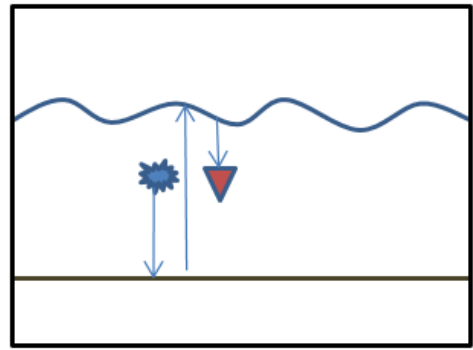
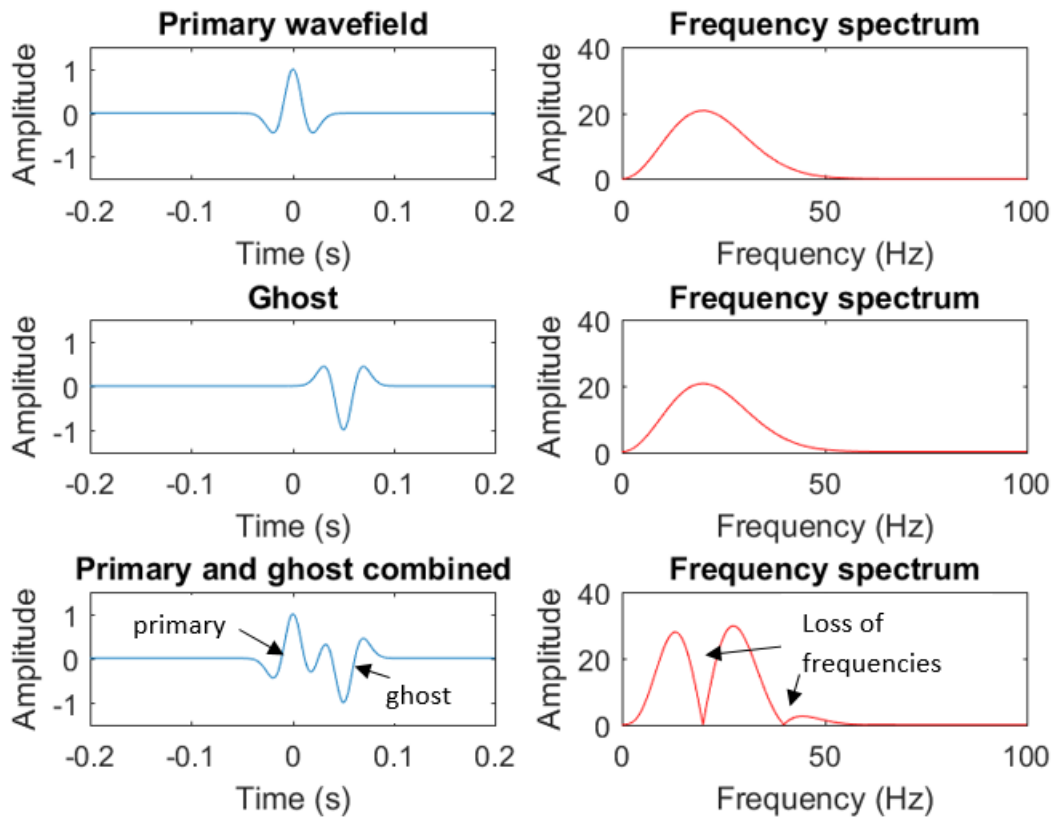


Figure 2-2: Receiver ghost

It is assumed that the total pressure wavefield at the free-surface is equal to zero, meaning that the up- and downgoing wavefields (or the primary and secondary wavefield) have opposite amplitudes.

Figure 2-3 shows an example of a primary wavefield (top) and a secondary (ghost) wavefield (middle) with reversed polarity and shifted in time with 0.05 seconds.



**Figure 2-3:** Example of a primary wavefield (top) and a ghost (middle) with reverse polarity and shifted in time. Combination of the two show a loss of frequencies (bottom).

Note how the frequency spectrum is distorted at specific frequency notches (0, 20, 40, 60 Hz) when the primary and ghost are added (bottom right fig. 2-3). As such, it can be seen that simultaneous recording of up- and downgoing wavefields lead to ghost notches to occur in the frequency spectrum of the recorded pressure wavefield.

Finally, it is remarked that a straightforward application of equation 2-11 to compute the deghosted upgoing pressure wavefield, leads to numerical instabilities when the denominator on the right-hand side approaches zero. For a constant receiver depth  $x_3^R$ , this occurs for distinct combinations of temporal frequency parameters and wavenumbers  $k_1$  and  $k_2$ .

In subsequent sections, two strategies are discussed to circumvent these numerical instabilities.

## 2-2 Acquisition-based deghosting

As discussed in the previous section, ghost events generate a complex set of interference patterns that are difficult to circumvent. One strategy to address the ghosts is to alter the

acquisition geometry. In literature, modifications to conventional acquisition geometries have been proposed to acquire data that allow for addressing the ghosts optimally during subsequent processing steps. These acquisition modifications either make use of multi-component recording sensors, where complementary data is used to remove the interference patterns (e.g. [Carlson et al., 2007] and [Vassalo et al., 2012]), or the shape of the recording streamers is altered, aiming to reduce the impact of the interference patterns as they become offset-dependent [Soubaras, 2010]. To address the source ghost, multi-level sources have been utilized (e.g. [Parkes and Hegna, 2011]).

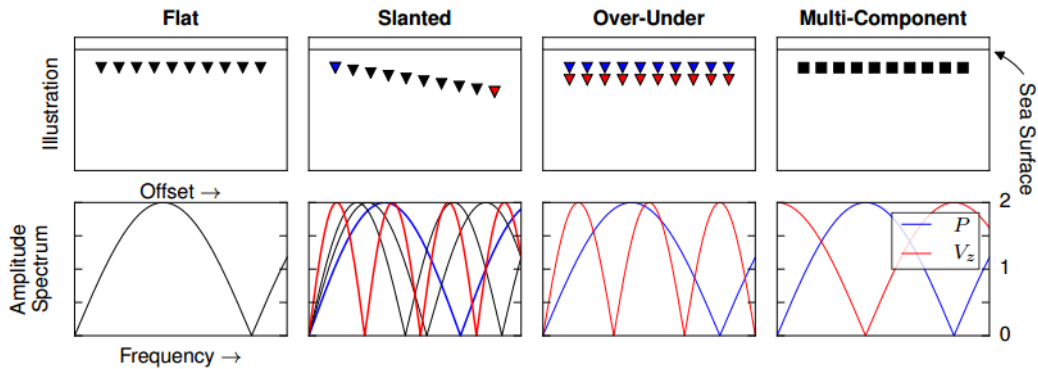


**Figure 2-4:** Different acquisition systems, figure from [Schubert, 2015].

The slanted streamer set-up (middle left figure 2-4) tows the streamer at a tilted angle causing the primary and ghost wavefield to enter the receiver at subsequently earlier and later times. The over-under set-up [Moldoveanu et al., 2006] (middle right figure 2-4) tows two receiver streamers, one is towed at a shallow depth causing the first ghost notch to occur at a high frequency. The second streamer is towed below the first streamer that will acquire a frequency spectrum with the initial frequency notches occurring at lower frequencies. Combining both profiles will average out the frequency spectrum. These acquisition set-ups do not come without a hurdle because they may be limited in availability and higher in cost. Additional processing steps may also be needed.

## 2-3 Processing-based deghosting

In processing-based solutions, no significant modifications to the data acquisition are made, aiming to recover data where the interference between up- and downgoing wavefields has taken place.

In recent years, processing flat streamer legacy data has become increasingly popular due to the interest in data with a greater bandwidth, the increase of computing power, and a better understanding of the ghost problem. Most processing-based methods utilize wavefield propagation operators that are based on the wave-equation, discussed earlier. In many implementations, a forward operator - that describes how any upgoing wavefield that is reflected by the free-surface will create a ghost - is inverted for (e.g. [Riyanti et al., 2008] and [Poole, 2013]). This inversion is not straightforward, as the inversion causes to enhance the noise present where notches occur. In Appendix 2, applications of direct inversion-based

deghosting operators are discussed, based on the 1D and 2D equivalents of the deghosting equation 2-11

An alternative approach to inversion-based deghosting is presented by [Ferber and Beasley, 2014], where a causal deghosting method is presented. Causality implies dependence on past and present inputs, not on their future inputs, where the latter is termed a-causality. The idea of towing a receiver beyond a certain depth, resulting in the ghost signal becoming invisible within the eventual target zone is utilized. The method recursively shifts out the downgoing ghosts by adding a water column in every new step that increases the distance of the receiver to the sea surface, keeping the distance of the receiver and subsurface the same. One limitation of the recursive nature of the method is that noise is gradually boosted within every step. An advantage is that it does not have the problem of having to divide by values (close to) zero. The technique requires exact knowledge of the receiver depth, propagation velocity in water and assumes a flat sea surface.

[Beasley et al., 2013] describe another causal deghosting method that utilizes the wave equation in the  $t-x$  domain. The method does not require estimating missing frequencies through statistical or other means in the spectral (frequency) domain. Assuming receiver depth, propagation velocity in water and other water surface properties are known, the wave equation is used to simulate propagation of the up- and downgoing wavefields between the receivers and the water surface to accomplish wavefield separation. The authors assume direct arrivals and other related noise are removed from the data, which is the norm for deghosting methods.

## 2-4 Sensitivity analysis

Inspection of equation 2-11 shows that, for deghosting to work, parameters such as the propagation velocity in water, the source- and receiver depths and the free-surface reflection coefficient (water surface reflectivity) need to be known. In practice, uncertainties can lead to ringing artifacts in the final result, these artifacts can be spurious signals that occur near sharp transitions in a signal. When deghosting with a deterministic approach, as discussed in the previous section, parameters are assumed that have certain values. When these values deviate too much from the actual values, ringing may occur. When for instance the receiver depth is assumed to be 19 m, instead of the correct value of 20 m, the ghost notches are not filled correctly and the resulting  $t-x$  plot indicates an erroneous result (fig. 2-5). The ringing result is clearly visible in the  $t-x$  plot (right figure).

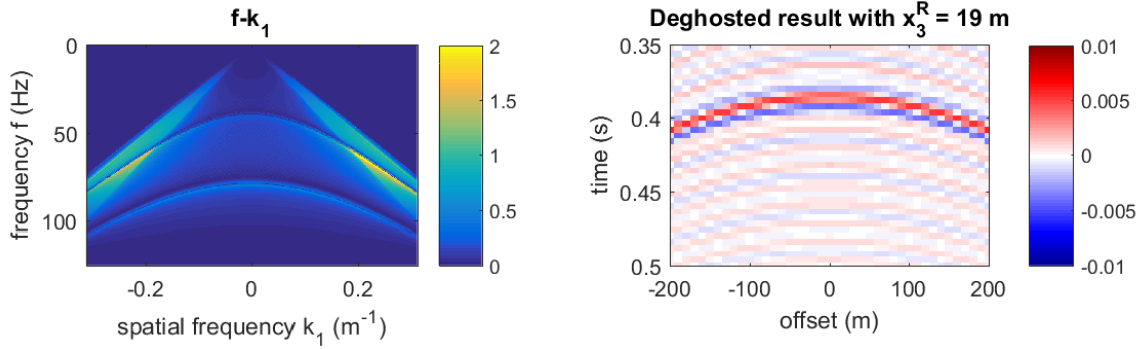


**Figure 2-5:** Deghosting with wrong receiver depth ( $x_3^R = 19$  m).

The figure below displays the occurrence of ringing when using a water surface reflectivity of  $-0.95$  instead of  $-1$ .

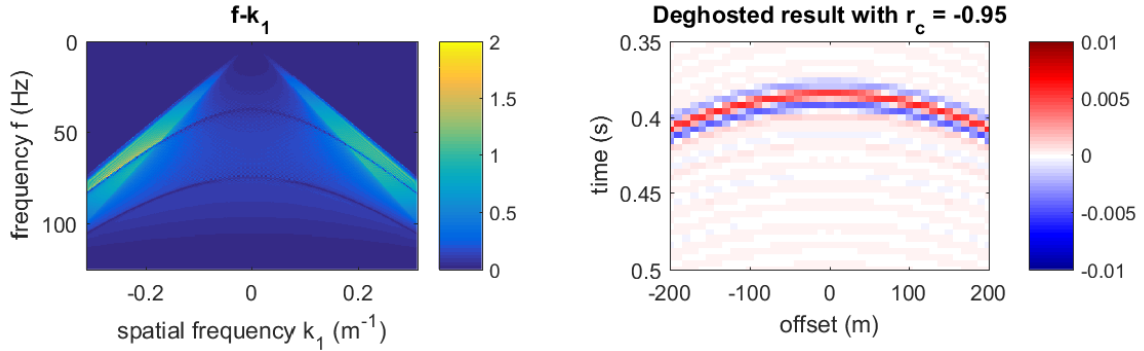


**Figure 2-6:** Deghosting with wrong water surface reflectivity ( $r_c = -0.95$ ).

A sensitivity analysis can provide insight into the sensitivity of changing a value for a model parameter (receiver depth, water surface reflectivity or propagation wave velocity in water) on the final result. The sensitivity analysis can be made using the mean square error (MSE), defined as

$$MSE = \frac{\|D - D_{REF}\|^2}{N_d} \quad (2-15)$$

where  $N_d$  is the number of data points. The mean squared error gives an indication of the goodness of fit of a proposed model ( $D$ ) and a reference model ( $D_{ref}$ ). In this case the reference model was taken to be the deghosted result in the  $f - k$  domain with the correct parameter values ( $x_3^R = 20$  m,  $r_c = -1$ ,  $c = 1500$  m/s). The proposed model would then be the deghosted result with a slight change in one deghosting parameter. The lower the MSE, the greater the similarity between the proposed model and the reference model, therefore indicating a lower sensitivity of the deghosting parameter when changed. In figures 2-7 ( $t - x$  domain) and 2-8 ( $f - k$  domain) a range of one hundred different receiver depths, water surface reflectivities, and propagation wave velocities are input into the model (steps of 1% change from the correct value taken). At the center of the range of values the MSE is zero, this is due to the fact that the parameter values of the proposed model match the reference model parameter values.

The range of values tested are:

Parameter	Correct value	Estimated values
$x_3^R$ (m)	20	10, 10.2, 10.4, ..., 29.8, 30
$r_c$	-1	-1.5, -1.49, -1.48, ..., -0.49, -0.5
$c$ (m/s)	1500	750, 765, 780, ..., 2235, 2250

**Table 2-1:** Range of values of receiver depth, water surface reflectivity and velocity used to compare with model.

In reality the water surface reflectivity does not become less than -1, for the sake of this analysis this fact has been discarded.

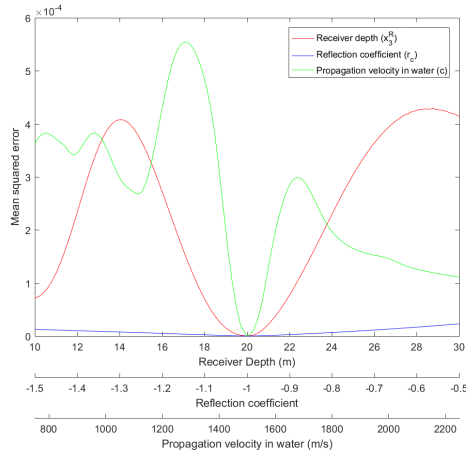


**Figure 2-7:** Sensitivity of result in  $t - x$  on deghosting parameters.

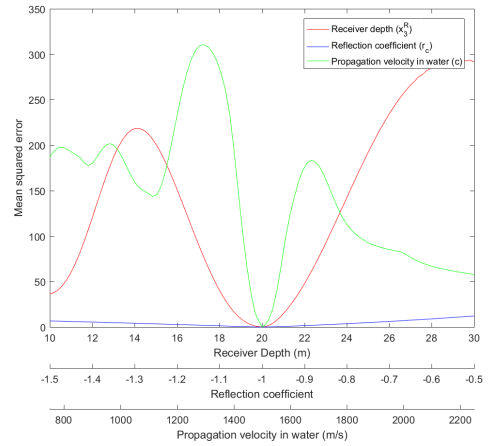


**Figure 2-8:** Sensitivity of result in  $f - k$  on deghosting parameters.

The two figures above display the change in the mean squared error ( $y$ -axis) when the values for the deghosting parameters ( $x$ -axis) are varied by 1% of the correct value. The figure on the left displays the MSE of the data in the  $t - x$  domain and the figure on the right in the  $f - k$  domain. Note that the difference between the  $t - x$  and  $f - k$  MSE plots lies in the range of the MSE (displayed on the  $y$ -axis). Both plots indicate that the propagation wave velocity in water (green line) is the most sensitive parameter when changing it by 1% of the correct value. The water surface reflectivity (blue line) is the least sensitive parameter. The receiver depth (red line) and propagation wave velocity in water show a strong non-symmetric relationship

when the values deviate up or down from the correct value in the center ( $x_3^R = 20$  m and  $c = 1500$  m/s). The water surface reflectivity is only slightly non-symmetric. The reader is referred to Appendix A, figure A4 on an illustration how varying deghosting parameters has an effect on the deghosting operator. Figure A12 displays another sensitivity figure for a slightly different range of parameter values.

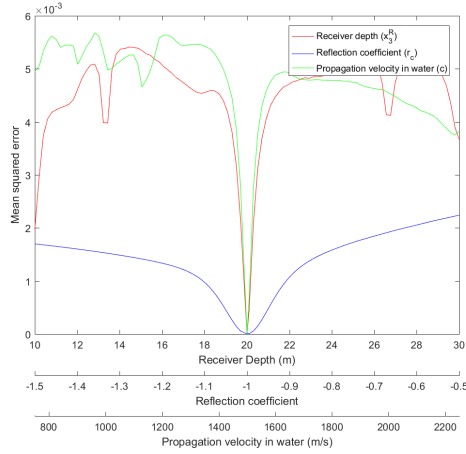


**Figure 2-9:** Sensitivity of result in  $t - x$  on deghosting parameters with 10 % noise present.

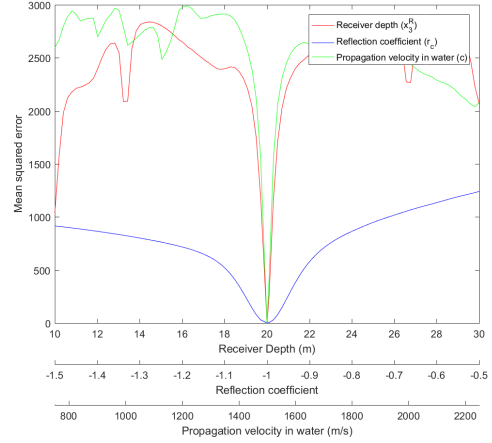


**Figure 2-10:** Sensitivity of result in  $f - k$  on deghosting parameters with 10 % noise present.

The two plots above (figures 2-9 and 2-10) illustrate the same concept as before except that 10% random noise is added. Adding noise results in a different behavior for all deghosting parameters, especially at deviations from 0-10%. The propagation wave velocity in water is still the most sensitive, the receiver depth does almost have the same sensitivity in the range of 19.5 m - 20.5 m when compared to the propagation wave velocity in water.

In reality, the propagation wave velocity in water ranges from 1480 m/s - 1520 m/s [Wong et al., 1995]. This velocity range depends on the pressure (which increases with depth), temperature (4 m/s change per 1 °C), and salinity (1 m/s change per 1‰). The receiver depth uncertainty may range from 0 - 2 m [Kragh et al., 2002] depending on the roughness of the sea (calm weather or storm). The water surface reflectivity ranges from -0.88 to -1 [Orji et al., 2013] and depends on the frequency and incidence angle of the wave. Referring back to the sensitivity figures, it can be stated that in reality the effect of a temperature change or salinity change will affect the deghosting severely when compared to a water surface reflectivity change. A rough sea will also degrade the deghosting performance, just slightly less than the propagation wave velocity in water.

The outcome of sensitivity studies indicate the necessity to circumvent the impact of uncertainty as part of seismic wavefield deghosting. In the next section, adaptive deghosting methods will be discussed as a means to achieve that.

## 2-5 Adaptive deghosting

As shown in the previous section, incorrect values for the deghosting parameters leads to ringing artifacts. The effect of ringing can be minimized through the use of an adaptive deghosting method. Multiple studies have been carried out that tackle the adaptive problem in a different way. In this section, a review is provided of a number of papers that are based on the idea of finding the assumed to be correct values for the deghosting parameters by minimizing or maximizing a norm/criterion. The norms used here are L1, L2 and Kurtosis, which are described in Appendix 1.

### 2-5-1 Single sensor adaptive deghosting (SSAD), Rickett et al. 2014

The adaptive deghosting method of [Rickett et al., 2014] is the only method that actually compares data and a model with assumed parameter values, and refines the model to match the data so the best parameter values are found. The technique can also be used for 3D propagation with arbitrary crossline dip and it works both for flat or variable-depth streamers. The algorithm attempts to decompose the data into a sparse set of plane-wave basis coefficients by minimizing an objection function.

$$\text{SSAD} : \min_{t_\Delta, \tilde{P}^{up}} \|\tilde{P}_{data} - \tilde{G}(t_\Delta)\tilde{P}^{up}\|_2^2 + \lambda\|P^{up}\|_1, \quad (2-16)$$

where the tilde symbol  $\tilde{\cdot}$  stands for an approximation,  $G(t_\Delta)$  is the ghost operator and lambda  $\lambda$  a stabilization factor (described in appendix A). The  $L_2$  norm describes the residual energy between the recorded data  $P_{data}$  and a proposed model that should fit the data. The  $L_1$  norm describes the sparsity of the synthetic upgoing wavefield. The second term aims to stabilize the inversion.

### 2-5-2 Energy minimization, Schubert 2015

[Schubert, 2015] took a closer look at eq. 2-16. It is found that there exists an up-going wavefield for any ghost delay time ( $t_\Delta$ ) that is consistent with the data. In other words, when finding a match between the data and a proposed model, the model can be made to match the data with any ghost delay time:

$$\|\tilde{P}_{data} - \tilde{G}(t_\Delta)\tilde{P}^{up}\|_2^2 \approx \|\tilde{P}_{data} - G(t_\Delta)\frac{1}{G(t_\Delta)}\tilde{P}_{data}\|_2^2 = 0. \quad (2-17)$$

The first term can therefore be neglected in equation 2-16. The idea is to minimize the second term ( $\|P^{up}\|_1$ ) resulting in a ghost delay with minimal ringing. It is shown that, when neglecting the first term, there is no degradation in performance compared to the SSAD method. The data is  $\tau - p$  transformed which simplifies the targeting of ghost delay times. A line search is performed of potential  $t_\Delta$  candidates and the ghost model is applied rapidly in the frequency domain (works because of Parsevals theorem). A limitation of this method is that it cannot estimate a ghost delay smaller than the reciprocal of the usable bandwidth. Besides that, ghosts may also originate from destructive interference of primary reflections, causing the possibility of a wrong minimum energy solution.

### 2-5-3 Adaptive windowed deghosting, Zhang et al. 2016

[Zhang et al., 2016] takes a similar approach as the paper from [Schubert, 2015]. The authors try different criteria ( $L_1$ ,  $L_2$ , and Kurtosis) to obtain the ghost-free primary. The  $L_1$  norm is used because its easier to calculate and behaves more robustly than either the Kurtosis or  $L_2$  norm, this has been shown using field data sets. The  $\tau - p$  domain is again used to apply the deghosting algorithm. This paper also adaptively searches for the water surface reflectivity which is a function of wave conditions, emergence angles and frequency.

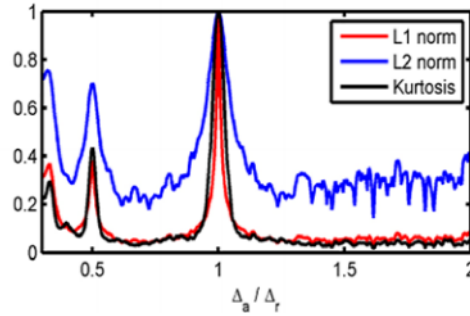


Figure 2-11: Finding delay-time using  $L_1$ ,  $L_2$ , and Kurtosis, figure from [Zhang et al., 2016].

### 2-5-4 Adaptive receiver deghosting for deep-tow pressure data, Mehdi et al. 2016

In [Aharchaou and Anderson, 2016], special attention is paid to stability factors to mitigate the effects of the instabilities occurring due to the ghost notch frequencies. The ghost delay can be estimated for each horizontal slowness and similar to other deghosting methods this paper uses the periodicity in the temporal frequency domain, where the ghosting effect creates notches that are regularly spaced by  $\frac{1}{t_\Delta}$  in the power (amplitude) spectrum. A periodic trend created by regular ghost notches can be emphasized by taking the log of the power spectrum. Taking the Fourier transform and the logarithm shows spikes at the ghost delays. The power cepstrum (log of amplitude) is related to the power spectrum which in turn is related to the autocorrelation, where the autocorrelation function (eq. 2-18) is the inverse Fourier transform of the power spectral density:

$$r(t) = \int_{-\infty}^{\infty} x(\tau)x(\tau + t)d\tau = F^{-1}S_{xx}(f) = F^{-1}|\hat{x}(f)|^2, \quad (2-18)$$

where  $F^{-1}$  stands for the inverse Fourier transform,  $S_{xx}$  the power spectral density,  $r(t)$  for the autocorrelation function, and  $\hat{x}(f)$  is the pressure data in the frequency domain  $P_{data}(f)$ . The useful trait of taking the logarithm is that multiplications become additions which is maintained through a Fourier transform. The algorithm is very easy to use, it requires only one FFT-based iteration to estimate the ghost delay and fill the notches more optimally.

### 2-5-5 Adaptive deghosting by Kurtosis maximisation, Grion et al. 2015

[Grion et al., 2015] take on a new approach, where they utilize the statistical kurtosis method by looking at the autocorrelation whilst shifting through different values of the water surface

reflectivity and the ghost delay. The autocorrelation with the highest Kurtosis value turns out to be the correct value for the estimated parameter (fig. 2-12).

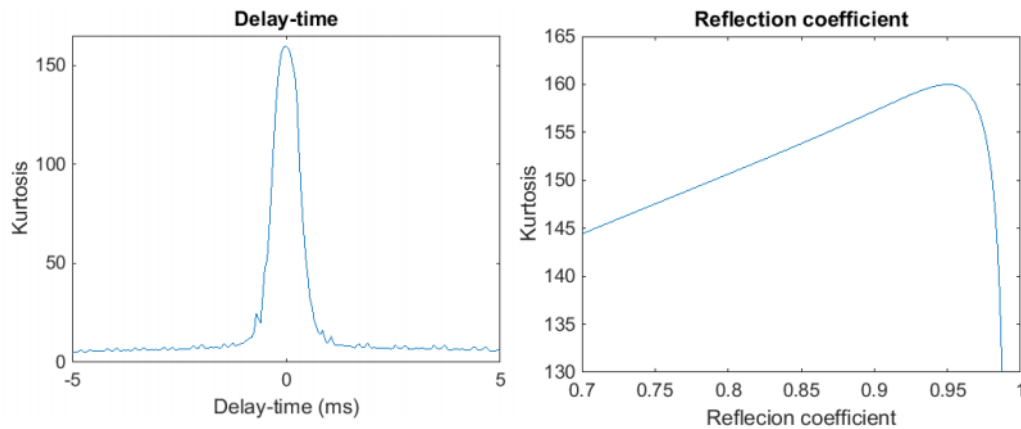


**Figure 2-12:** Finding delay-time and water surface reflectivity using Kurtosis of the autocorrelation, figure from [Grion et al., 2015].

### 2-5-6 Premigration deghosting for marine streamer data using a bootstrap approach in Tau-P Domain, Wang et al. 2013

The paper from [Wang et al., 2013] presents a method that uses a bootstrap approach (a statistical re-sampling method) with a  $\tau - p$  transform to estimate ghost delays and remove receiver ghosts from seismic data. The method reconstructs the ghost-free data through a least squares ( $L_2$ ) approach using inverted ghost delay times obtained from bootstrap iterations.  $\tau - p$  windows and a mirror migration is used to search for the ghost delay and upgoing wavefields.

### 2-5-7 Hydrophone-only receiver deghosting using a variable sea surface datum, King and Poole 2015

[King and Poole, 2015] have come up with a method to make an estimate of a sea surface profile. This method differs slightly from the usual adaptive methods where the ghost delay time and water surface reflectivity are found. The method extrapolates upcoming primaries past the sea surface to align them with the mirrored ghosts. When the mirrored ghost and extrapolated primary perfectly align there is a perfectly flat sea surface but when they don't there is an undulating surface. Cross correlating these two signals will give information on the time difference.

## 2-6 Summary

In this chapter the mathematical framework for ghost and deghosting has been given. Analysis shows the above adaptive deghosting methods all work in their own fashion, where there

is usually a similarity in the technique used to pick the most probable values for the deghosting parameters. It is shown that an uncertainty analysis into how accurate the picks of the deghosting parameter values is missing. In the next chapter a recently new deghosting technique called echo deblending will be discussed. This method forms the basis for further development, allowing for a new picking method for the water surface reflectivity and the receiver depth to be incorporated. Also, the pertaining implications for uncertainty analysis will be discussed.

---

## Chapter 3

---

# Echo deblending

Echo-deblending is a relatively new deghosting concept. In 2015, Berkhout and Blacquiere wrote their first paper on source deghosting as a special case of deblending [Berkhout and Blacquiere, 2015]. The idea behind blending is to simultaneously shoot multiple sources at different spatial locations so that their responses overlap and 'blend' with each other, thereby reducing the total acquisition time. Deblending is the process which retrieves the response of each individual source afterwards. This process uses a non-causal, full-wavefield algorithm. Source deghosting can be achieved by treating the source ghost as the result of a blended source. In this thesis we do not consider multiple sources but multiple receivers - the receiver ghost  $P^{down}(x_3^R; x_3^0)$  is considered to be recorded by a second virtual receiver, which can be thought of as a mirrored version of the normal receiver, with reversed polarity  $P^{down}(-x_3^R; x_3^0)$  (figure 3-1). The combination of the ghost and primary wavefield can be considered as a blended record and deblending will separate these two wavefields, thereby obtaining the requested deghosted result.

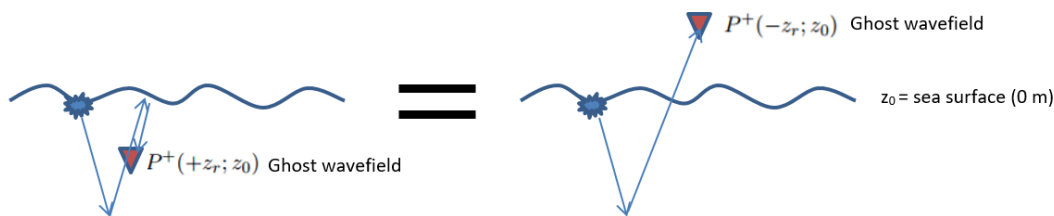


**Figure 3-1:** Receiver ghost wavefield expressed as a mirrored receiver ghost wavefield.

In the next section, the echo-deblending process will be explained and illustrated step by step using synthetic data of a primary wavefield and its corresponding ghost wavefield. The source is assumed to be at the free surface ( $x_3^0 = 0$  m) and the receiver at a depth of 20 m below the sea.

### 3-1 The algorithm

The algorithm starts by setting the initial estimates of the primary wavefield  $[P^{up}(x_3^R; x_3^0)]^{(0)}$  and its ghost wavefield  $[P^{down}(-x_3^R; x_3^0)]^{(0)}$  to the measured data  $P_{data}(x_3^R; x_3^0)$  (fig. 3-2):

$$[P^{up}(x_3^R; x_3^0)]^{(0)} = P_{data}(x_3^R; x_3^0), \quad [P^{down}(-x_3^R; x_3^0)]^{(0)} = P_{data}(x_3^R; x_3^0). \quad (3-1)$$

The brackets indicate an estimation and the superscript (0) indicates the first iteration of the algorithm.

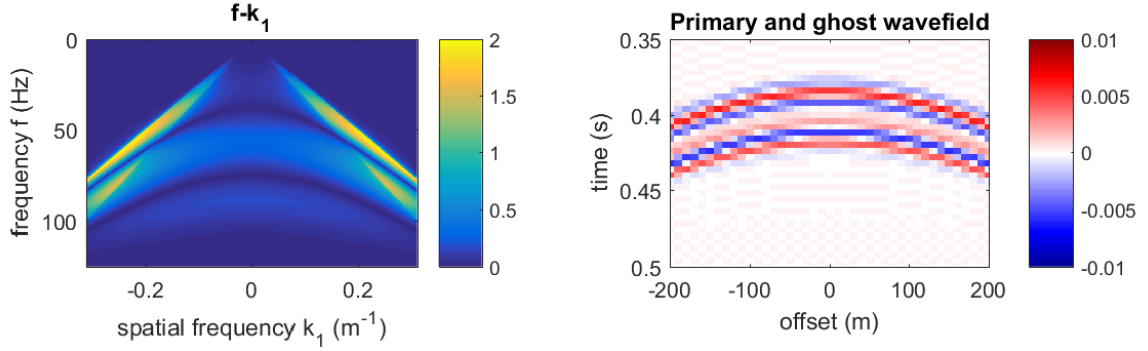


**Figure 3-2:** The raw data is used as initial estimates of the primary and ghost receiver wavefields.

The forward extrapolation operator  $W^-(x_3^0, x_3^R)$  is applied to the initial estimate of the primary wavefield to obtain the corresponding wavefield at the sea level  $[P^{up}(x_3^0; x_3^0)]^{(0)}$ , as follows

$$[P^{up}(x_3^0; x_3^0)]^{(0)} = W^-(x_3^0, x_3^R)[P^{up}(x_3^R; x_3^0)]^{(0)}, \quad (3-2)$$

which will bring the actual receiver from  $x_3^R$  m to  $x_3^0$  m, but it will also bring the ghost receiver from  $-x_3^R$  m to  $-2x_3^R$  m (see fig. 3-3).

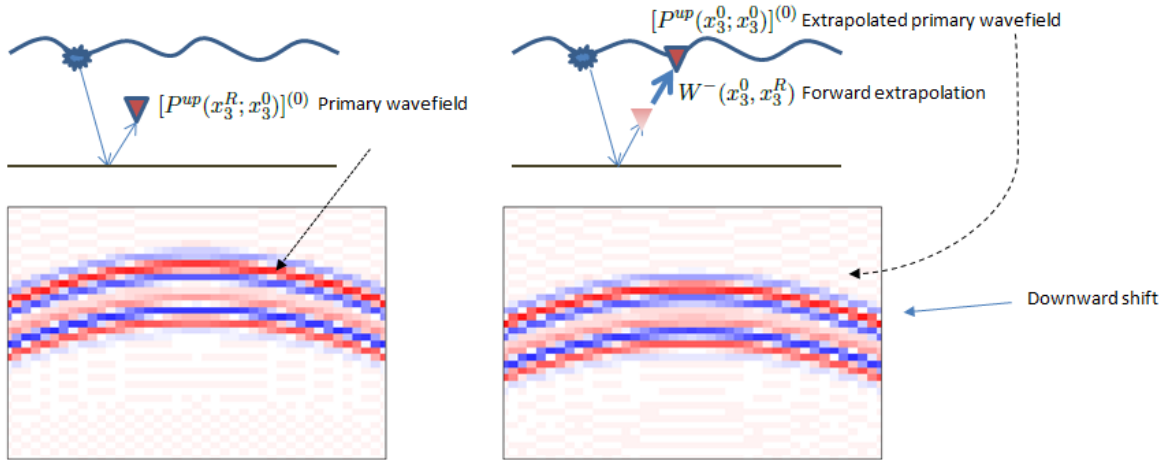


**Figure 3-3:** Estimate of primary wavefield at sea level obtained after forward extrapolation; the wavefield arrives later than before.

Application of the backward extrapolation operator  $F^+(x_3^0, -x_3^R)$ , and a polarity change ( $r_c$ ) to the data gives an estimate of the ghost wavefield at the sea level  $[P^{down}(x_3^0; x_3^0)]$ , (figure 3-4). The water surface reflectivity is assumed constant in this algorithm, in reality this may be a factor of frequency and incidence angle.

$$[P^{down}(x_3^0; x_3^0)]^{(0)} = r_c F^+(x_3^0, -x_3^R) [P^{down}(-x_3^R; x_3^0)]^{(0)}. \quad (3-3)$$

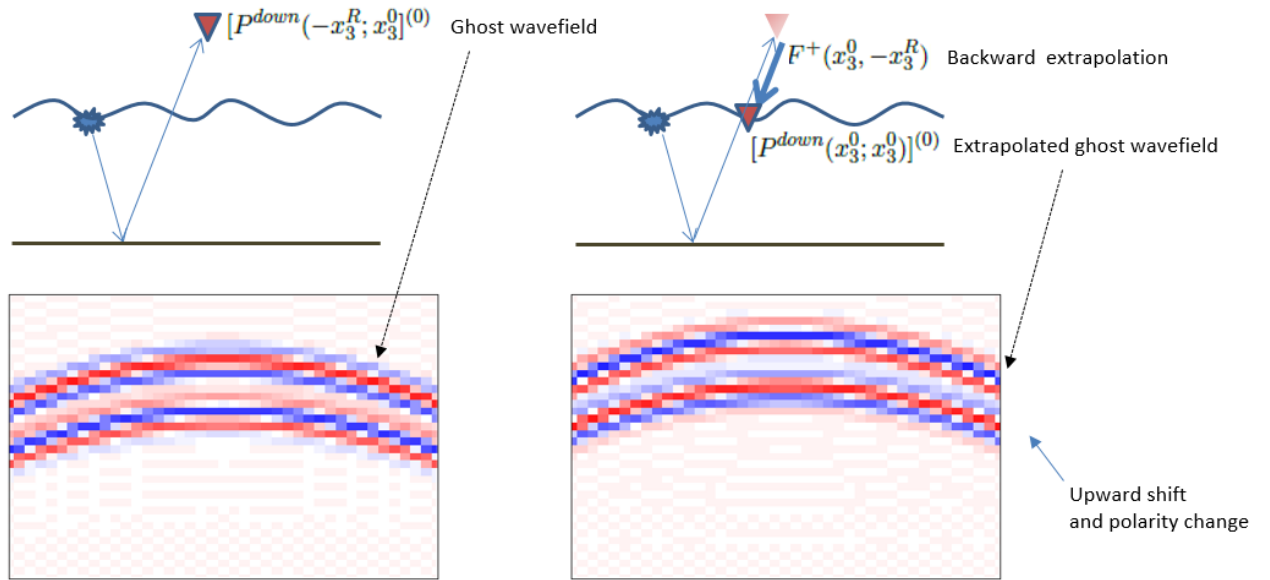


**Figure 3-4:** Estimate of ghost wavefield at sea level obtained after backward extrapolation; the wavefield arrives earlier than before.

The next step is to sum the estimates of the extrapolated primary and extrapolated ghost wavefields and to multiply this result by half (fig. 3-5):

$$[P(x_3^0; x_3^0)]^{(i)} = \frac{1}{2} [W^-(x_3^0, x_3^R) [P^{up}(x_3^R; x_3^0)]^{(i-1)} + r_c F^+(x_3^0, -x_3^R) [P^{down}(-x_3^R; x_3^0)]^{(i-1)}], \quad (3-4)$$

where the superscript (i) indicates the iteration step. This result contains the (desired) response of a source at  $x_3^0$  recorded at  $x_3^0$  together with some (undesired), lower amplitude, artificial events on the sides.

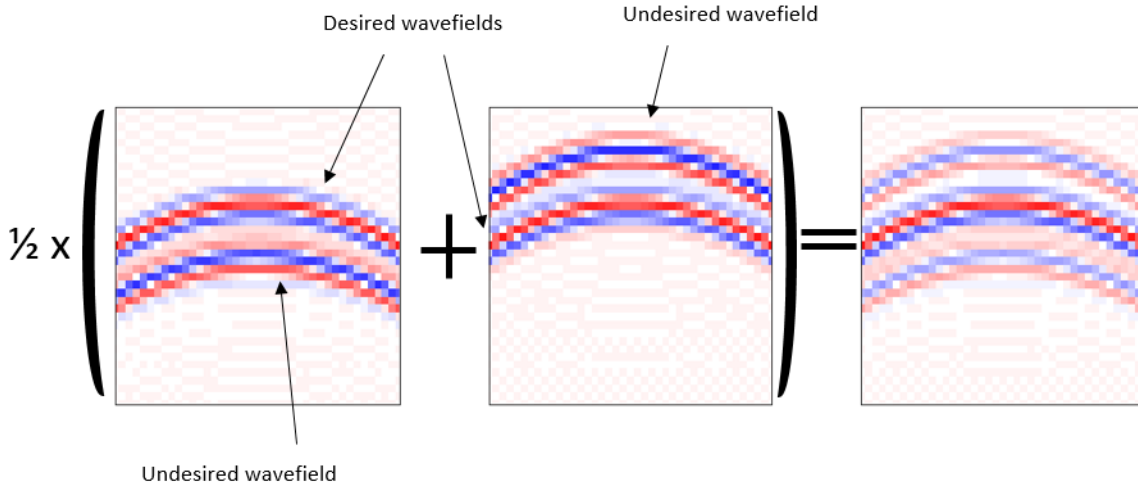


**Figure 3-5:** Summing and halving of forward and backward extrapolated wavefields.

The next step is remove any energy that falls below a certain threshold. The aim is to choose a threshold that will keep the desired wavefields and remove the undesired wavefields. The starting threshold is user dependent and is typically taken around half the energy of the maximum value of the original wavefield. Values of the original summed wavefield that fall below the threshold are discarded and the remaining values are stored in a new threshold data matrix. The equation below displays how the threshold works:

$$[P(x_3^0; x_3^0)_{threshold}]^{(0)} = \begin{cases} 0, & \text{if } |[P(x_3^0; x_3^0)]^{(0)}| < threshold \\ |[P(x_3^0; x_3^0)]^{(0)}| & \text{if } |[P(x_3^0; x_3^0)]^{(0)}| \geq threshold. \end{cases} \quad (3-5)$$

After thresholding, the backward extrapolation operator is applied to the resulting data to obtain a first estimate of the primary (that is ghost-free) response of a receiver at the actual receiver depth:

$$[P^{up}(x_3^R; x_3^0)]_{extr}^{(i)} = F^+(x_3^R, x_3^0)[P(x_3^0; x_3^0)_{threshold}]^{(i)}. \quad (3-6)$$

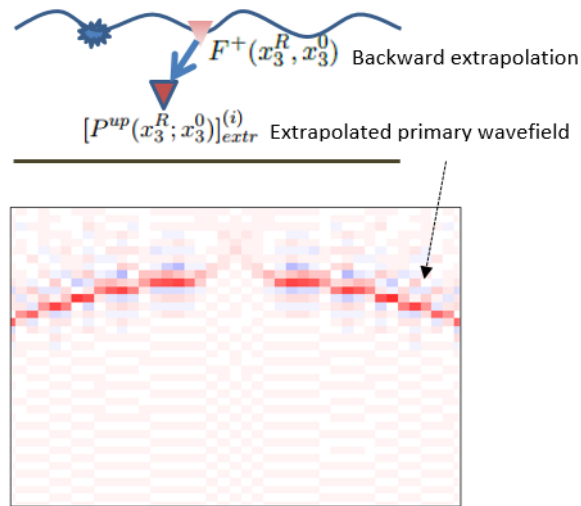


Figure 3-6: Backward extrapolation of data after thresholding.

Similarly, we apply the forward extrapolation operator to the data after thresholding and multiply with the water surface reflectivity to obtain a first estimate of the corresponding ghost wavefield for a receiver at the actual receiver depth.

$$[P^{down}(-x_3^R; x_3^0)]_{extr}^{(i)} = r_c W^-(-x_3^R, x_3^0) [P(x_3^0; x_3^0)_{threshold}]^{(i)}. \quad (3-7)$$

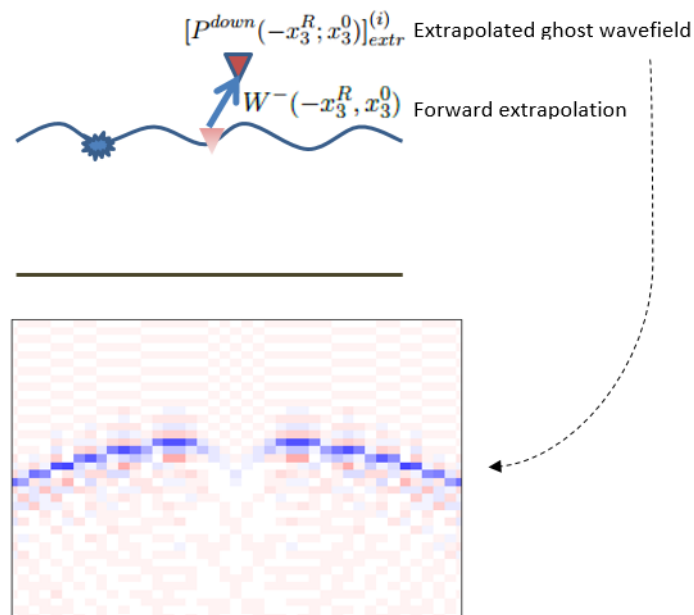
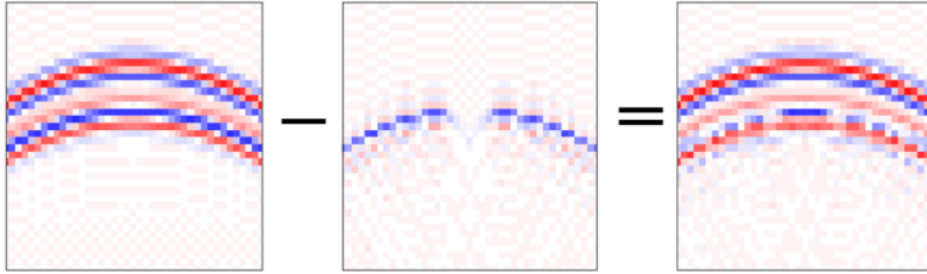
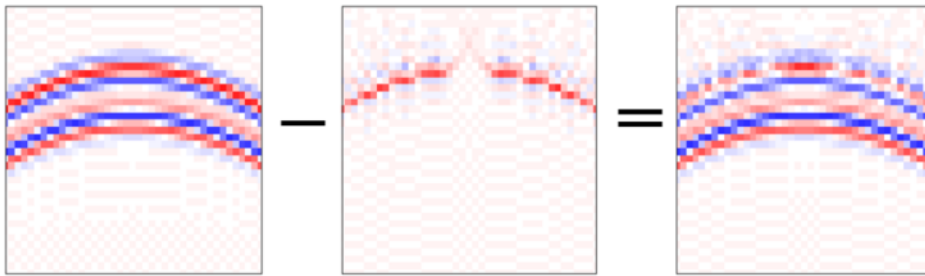


Figure 3-7: Forward extrapolation of data after thresholding.

These first estimates are subsequently (adaptively) subtracted from the actual data to obtain new estimates of the up-going primary wavefield and down-going ghost wavefield as the last step in an iteration. These wavefields are shown in figures 3-8 and 3-9.



**Figure 3-8:** New estimate of the up-going primary wavefield.



**Figure 3-9:** New estimate of the ghost wavefield.

The amplitude threshold is lowered in subsequent iterations until no improvements are obtained. The lack of further improvements is governed by the use of one or more stopping criteria. Note that these criteria are not always straightforward. For some discussion on this topic see for instance [Barret et al., 1994].

A residual is calculated after each iteration that will be utilized to stop the iterative process. The residual is defined as:

$$Residual^{(i)} = ([P^{down}]_{extr}^{(i)} + [P^{up}]_{extr}^{(i)}) - P_{data}. \quad (3-8)$$

The residual is recalculated in every iteration of the loop, considering the approximations of the primary and ghost wavefields improve in every new loop, as a result the residual decreases in every iteration.

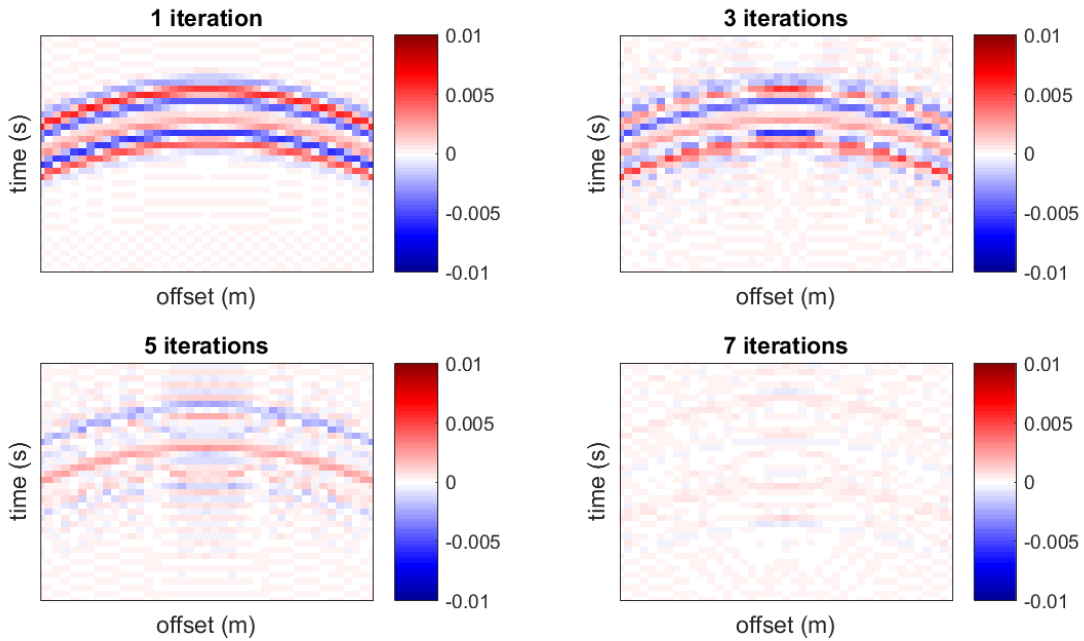


**Figure 3-10:** Residual after 1, 3, 5 and 7 iterations.

After a certain point, the decrease of the sum of the absolute values of the residuals (SAR) in one loop will be minimal when compared to the first decrements. One of the stopping criteria will be based upon the SAR. The following figure displays the sum of all the residuals in every iteration.

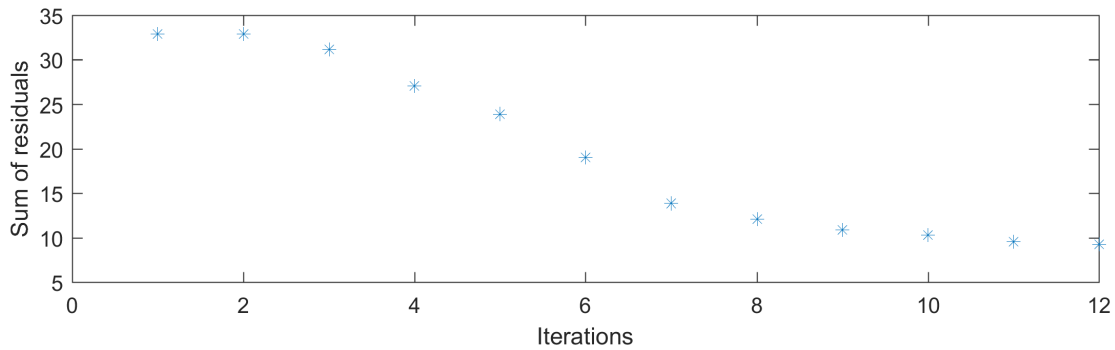


**Figure 3-11:** Behaviour of the SAR with iteration when using amplitude thresholding.

Before initiating the stopping criteria, five iterations of the algorithm are run. This is implemented to ensure if any discrepancies occur at the beginning of the algorithm (e.g. thresholding energy not sufficient at initiation), the iterative process endures to ensure proper deghosting. Two stopping criteria are used simultaneously. The first one is defined as:

$$S_{crit_1} = \sum |residual^{(i)}| < \sum |residual^{(i+1)}|. \quad (3-9)$$

The above equation indicates that if the residual of a new loop is greater than the residual of the previous loop, the loop process stops. The second criterion is:

$$S_{crit_2} = \frac{\sum |residual|_{L_i} - \sum |residual|_{L_{i+1}}}{\sum |residual|_{L_i}} < 0.1\%, \quad (3-10)$$

which expresses that a change of less than 0.1% in the residual compared to that of the previous iteration, will stop the process. This 0.1% value has been empirically deduced through several tests utilizing the echo-deblending algorithm. The complete iterative process is summarized in the diagram below.

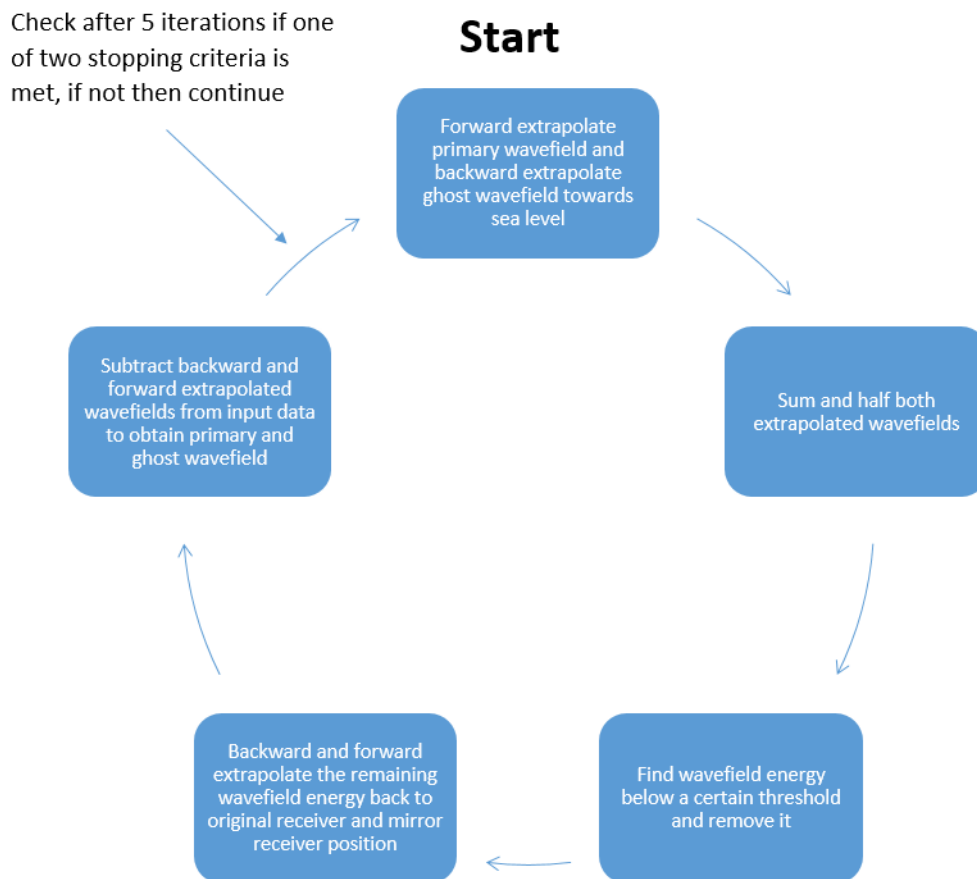


**Figure 3-12:** Loop diagram describing iterative echo-deblending.

Figure 3-13 below displays the  $f - k_x$  (left) and  $t - x$  (right) result of the echo-deblending algorithm after several iterations (1, 3, 5 and 7).

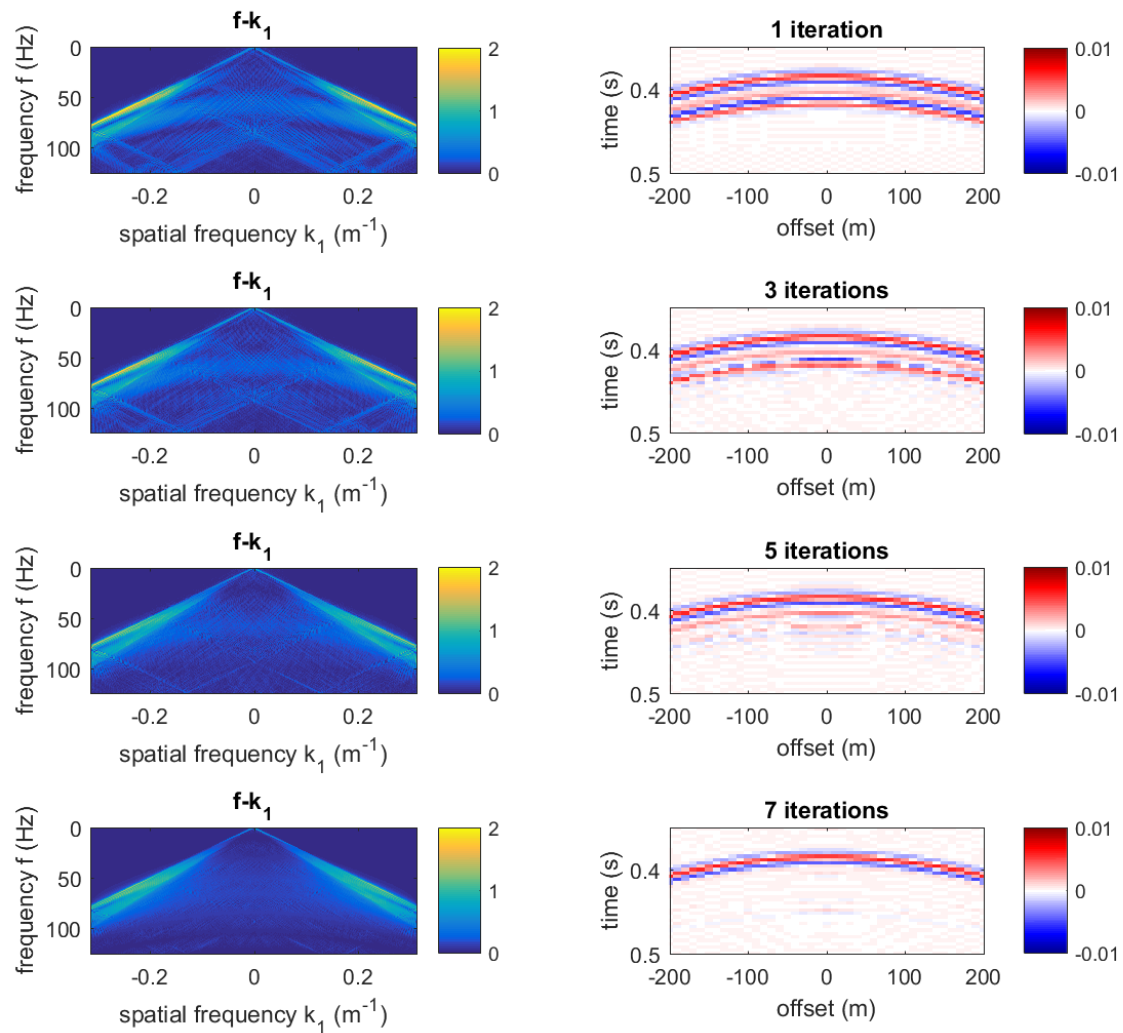
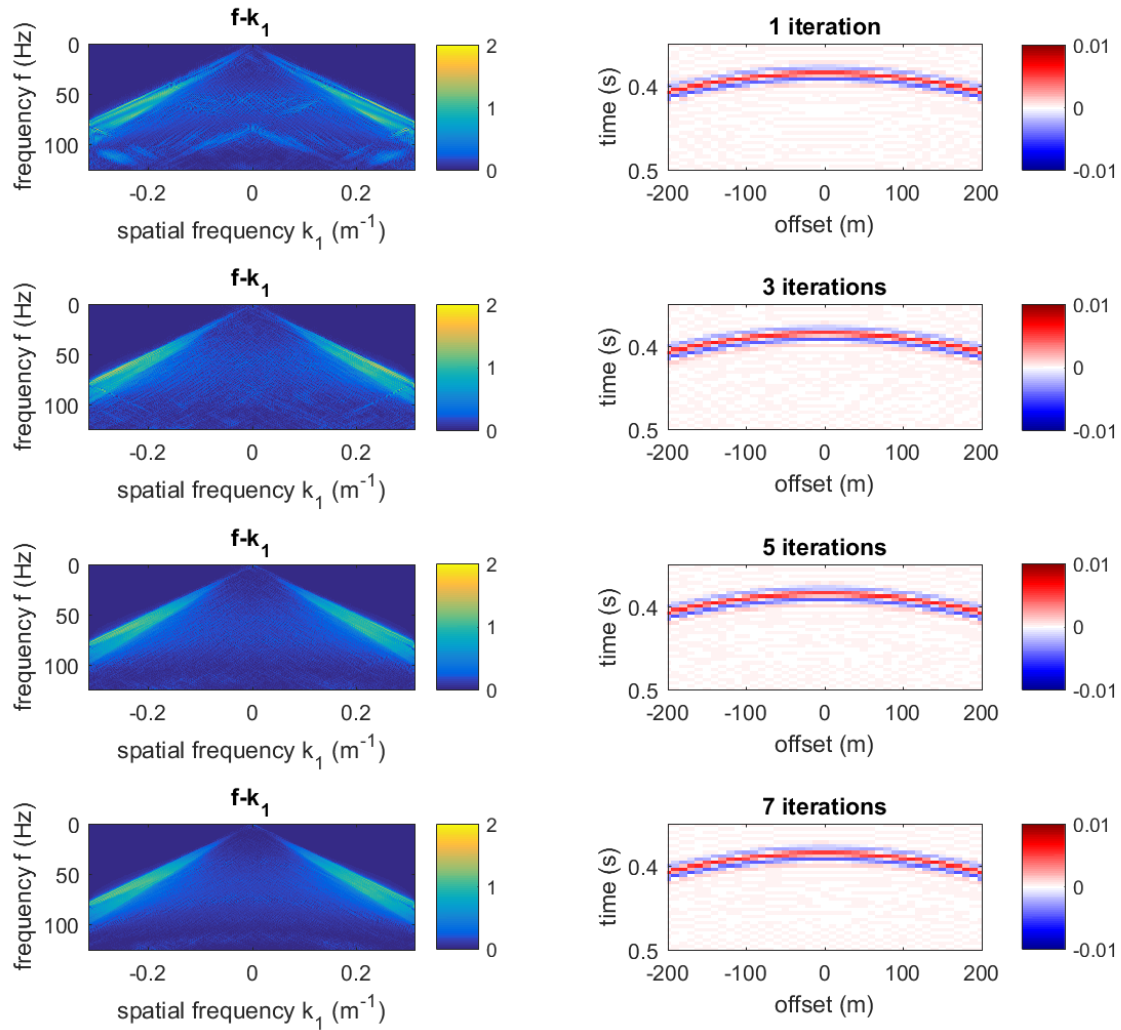


Figure 3-13: Upward going wavefield after 1, 3, 5 and 7 iterations using amplitude thresholding.

## 3-2 Coincidence filtering

A recently published modification [Yoo et al., 2017] combines the amplitude thresholding with travel-time matching to ensure that only events which are similar in amplitude (energy level) are selected in both extrapolated results, thereby improving the deblending process. Additionally, after every iteration of the looping process, the residual result is input into the loop (fig. 3-12) as if it were a primary and ghost wavefield. The full five steps of the loop are executed and the resulting backward and forward extrapolated residual - seen as artefacts - are subtracted from the total wavefield alongside the upward and downward going wavefields. This effectively attenuates artifacts. The threshold is derived from the difference in

amplitude. Figure 3-14 displays the result of the echo-debrending algorithm utilizing the coincidence filtering approach. The  $f - k_x$  spectrum is clearly ghost-free after 3 iterations whilst the amplitude thresholding result displayed this ghost-free result after 7 iterations.



**Figure 3-14:** Upward going wavefield after 1, 3, 5 and 7 iterations using coincidence filtering.

Figure 3-15 displays the SAR per iteration.

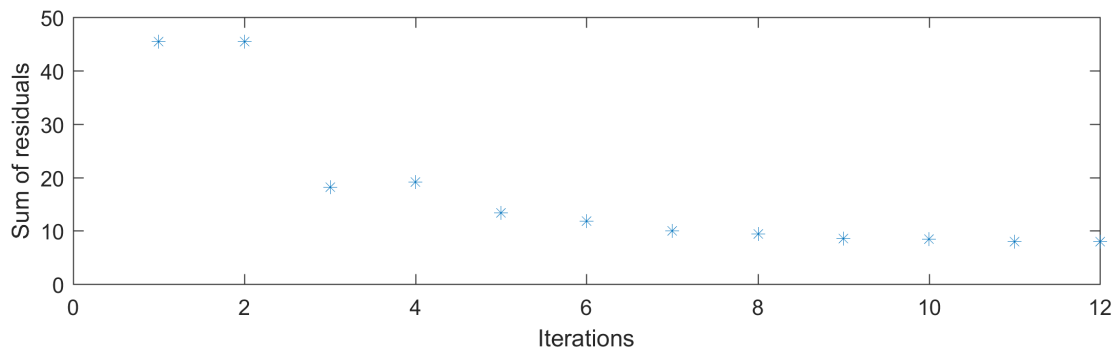


**Figure 3-15:** Behaviour of the residual with iteration when using coincidence filtering instead of amplitude thresholding.

In this chapter, echo-deblending was derived assuming that all necessary information, such as the receiver depth, is known beforehand and correct. In the next chapter, a modification is presented that allows echo-deblending to go from a deterministic method to an adaptive method and thereby to retrieve additional information.



# Adaptive echo-deblending with coincidence filtering

In previous chapters, deghosting and adaptive deghosting methods have been discussed. Several adaptive deghosting methods have been proposed but a quantitative uncertainty analysis seemed to be missing. Echo deblending provides an elegant framework to incorporate adaptivity because it is based in the t-x domain which allows event based analysis. In this chapter the extension of echo-deblending is developed that utilizes the residual result into a new method called adaptive echo-deblending (AED). Focus is put on estimating the water surface reflectivity and receiver depth. Standard deviation measurements are presented that help quantify the accuracy of the results obtained.

A very simple example will be used to illustrate various aspects of the AED method in the next three sections. The synthetic dataset used for this example contains an event at 300 m and is modeled with a constant receiver depth (20 m), water surface reflectivity (-1), and pressure wave velocity in water (1500 m/s).

### 4-1 Minimizing residuals

To recall, the residual was defined in equation 3.4 as:  $Residual = (P_{extr}^{down} + P_{extr}^{up}) - P_{data}$ . A low residual indicates that the difference between the input data and the combined upward and downward (ghost) wavefield is very small. In other words, the echo deblending algorithm has successfully separated the upward and downgoing wavefield, i.e. deghosted the data. If the echo deblending algorithm is run with a different receiver depth or water surface reflectivity, the result becomes prone to ringing, hence causing the residual to be higher. The example dataset was tested for a range of receiver depths (18 m - 22 m, with increments of 1% i.e. 0.2 m) using the echo-deblending algorithm. As it is difficult to compare two residuals directly or their individual values, and like the first stopping criterion, instead the sum of absolute residuals (SAR) will be used for comparison purposes. The corresponding behaviour of the residual for the range of receiver depths is shown in figure 4-1.

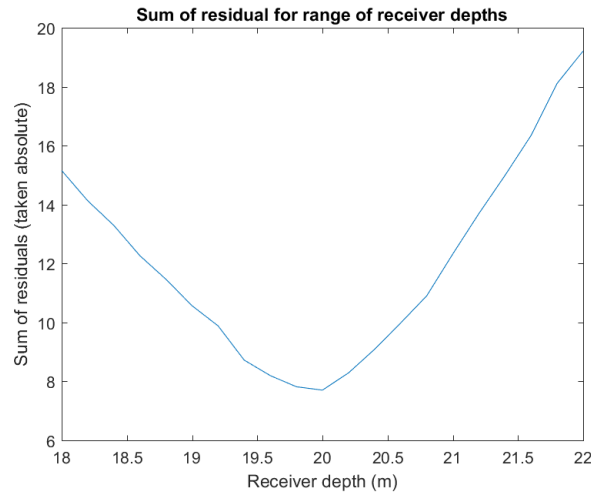


**Figure 4-1:** SAR for range of receiver depths (18 m - 22 m in steps of 0.02 m).

The figure shows that the lowest SAR is found for 20 m receiver depth, which corresponds to the receiver depth used to model the dataset. The residual can therefore also be used to determine the most probable or effective receiver depth and water surface reflectivity values. In principle we could test a range of values, determine the residual and for every single sample determine the value which delivers the lowest residual. The result would vary a lot between neighbouring traces and/or samples due to the presence of noise and other causes of errors. Regardless of the exact slope of a towed streamer, and even in rough seas, the effective depth should vary relatively smoothly. Comparing all the residual values at every single sample and offset would also be a very time consuming and costly process. Taking a wider spread of residual values (into account simultaneously) will average out any of these outliers and deliver a better representation of the actual receiver depth. The next section will therefore discuss an approach with user defined windows.

## 4-2 Windowing

A method is introduced that will use windowing whereby in each window a single value for every parameter will be estimated. An equivalence of the SAR, the average of the residuals, will be calculated per window. The average of the residuals is utilized to simplify the understanding of the uncertainty analysis presented in section 4-4. The windows overlap each other. This results in an interpolation between windows giving an averaged representation of every relevant parameter. The size of the window determines the amount of smoothing or accuracy in the end result. The process to determine the unknown receiver depth, utilizing windows, is summarized in the following steps:

- The echo deblending algorithm is run for a range of receiver depths (18 m to 22 m with steps of 1% i.e. 0.02 m) and the residual per run is stored in a matrix. The other parameters are assumed to be known and are kept constant.
- An odd sized window is defined (e.g. 3 x 3 units [traces x samples]) that will be used to run over the columns and rows of the residual matrix.

- For each window, the average of the residuals is computed for the respective receiver depths. The receiver depth that corresponds to the window that contains the minimum average residual is stored in a new window with the same size. This new window is weighted through multiplication with a pyramid (bottom LHS and RHS figure 4-2).
- The window slides to the right, with a length half its width and is rounded down (e.g. window size: 3 => halved and rounded down = 1). The new window will overlap two thirds of the earlier window and lies on one third of a new region (fig. 4-2). The previous step is carried out and the resulting pyramid is superimposed with the previous pyramid.
- The window keeps sliding to the right, repeating the step above until it reaches the side of the matrix. At this point the window travels back to the beginning but shifts one row down below the first window. Again, the new pyramids are subsequently superimposed with the overlapping other pyramids. This process is repeated until the end of the residual matrix.
- To prevent edge effects, the original matrix size is increased beforehand by the width of a window on each side. The average receiver depth of the tested range is input as value in these artificial sides. Once the process is complete the artificial sides are removed.

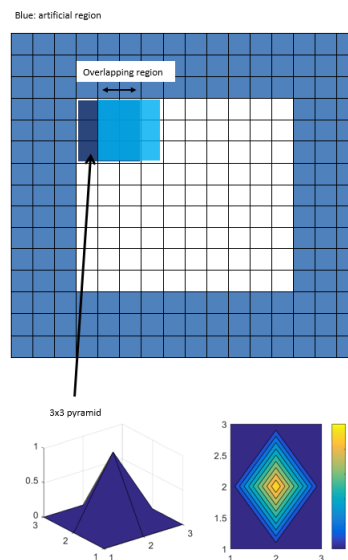


**Figure 4-2:** Pyramid sliding

The final result is an effective receiver depth map (LHS fig. 4-3). Note that if all windows contained the same depth, the combination would result in the same constant value everywhere. The algorithm utilizes a window of 51x51. Every point in the figure provides an estimate of the receiver depth at a specific offset and time. Considering there is only one event in this dataset, the effective receiver depth map is scaled by an energy factor that will ensure the event stands out from any background noise (middle LHS figure). The middle RHS figure displays where the method has obtained the exact receiver depth (20 m). It appears that

the AED method only retrieved the proper depth for a small part near the top left of the apex. To verify whether the AED method was close to obtaining the correct receiver depth a  $\pm 5\%$  margin is taken into consideration (RHS figure). The results are far more promising utilizing this 5% margin.

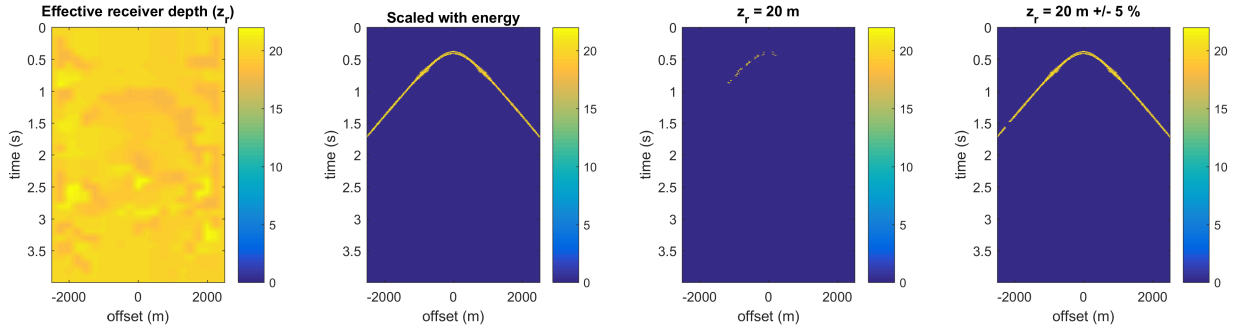


Figure 4-3: Obtaining receiver depth, tested with  $z_r = 18 \text{ m} - 22 \text{ m}$ .

The same process is executed to obtain an effective water surface reflectivity map. The tested range of water surface reflectivities was  $-1$  to  $-0.7$  with increments of  $1\%$  i.e.  $0.01$ . Figure 4-4 displays the results of the method on obtaining the correct water surface reflectivity. Similar to Figure 4-3, we again use a  $5\%$  margin to obtain a better representation of the result.

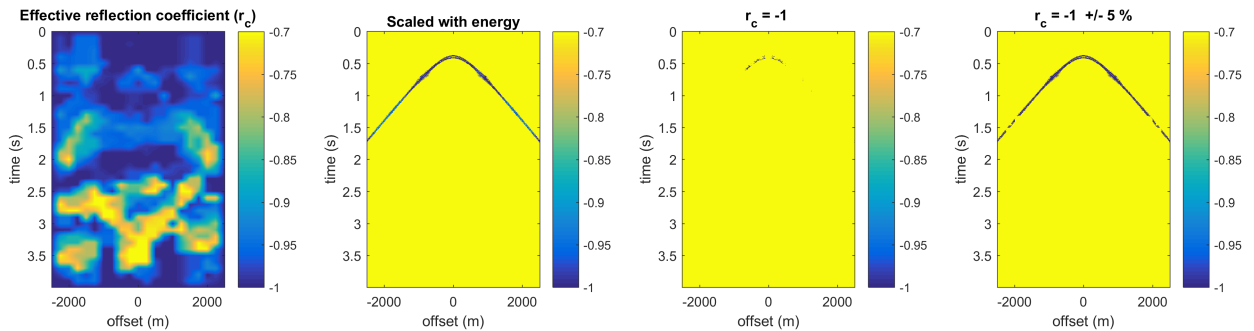


Figure 4-4: Obtaining water surface reflectivity, tested with  $r_c = -1, -0.99, \dots, -0.7$ .

The AED result on obtaining exact parameter values for a single event - whilst keeping all parameter settings constant - was not sufficient. Utilizing a  $5\%$  margin into the AED method delivered the expected outcome. In section 4-4 we will introduce the standard deviation of the residuals per window to provide an additional way of illustrating and quantifying the accuracy of the results.

### 4-3 Event tracking

The user is sometimes only interested in specific events of a dataset. An event tracking method is introduced that will allow the user to track the effective receiver depth or water surface reflectivity over one specific event. This can lead to reduced computing cost and run-time. Also, if the signal-to-noise ratio is low on average but sufficiently large in specific

areas, then the method can be used to focus on events in these areas to obtain meaningful results. Additionally, the method can be used for specific quality checks.

The method is based upon knowing the specific times of events. The times of an event of interest are provided to the method via a header of the data. The event tracking method utilizes windows similar to the AED method. To ensure the windows interpolate correctly over the whole event, the number of windows that span the event is calculated using the following equation:

$$Windows = 2\left(\frac{n_r}{L_{window}}\right) - 1, \quad (4-1)$$

where  $n_r$  is the number of receivers,  $L_{window}$  is the length and width of the window. The same technique to obtain the effective parameter values utilizing minimum residuals is applied. The end result is an averaged representation of the tested effective parameter. This method is utilized in section 4-7 to get a better view of the specific effective parameters tested.

## 4-4 Uncertainty analysis

To give an indication of the accuracy of the result of the AED algorithm, the standard deviation for each of the residuals per window corresponding to the effective parameter value obtained is presented. The standard deviation is a measure that is used to quantify the amount of variation or dispersion of a set of data values, mathematically it is defined as:

$$SD = \sqrt{\frac{1}{N-1} \sum_{i=1}^N |A_i - \mu|^2}, \quad (4-2)$$

where  $\mu$  is the average of the residuals in the window,  $N$  the total number of data points in the window, and  $A_i$  the residual at one point. A low standard deviation suggests that the estimate is more reliable. To illustrate the effect of choosing a wrong receiver depth on the standard deviation result, two different AED runs are executed. One run tests a single receiver depth of 18 m (figure 4-5) and the other (figure 4-6) tests a range of receiver depths from 18 m to 22 m (similar to the previous example), where the correct receiver depth (20 m) is obtained.

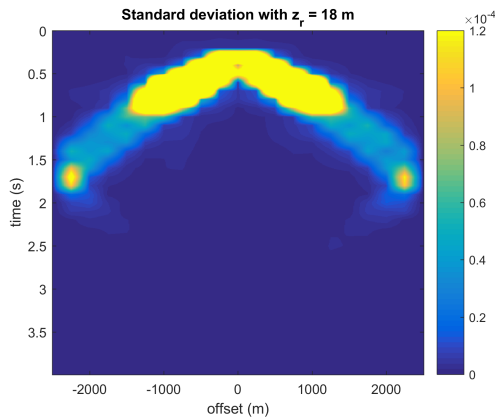


**Figure 4-5:** Standard deviation, wrong effective receiver depth ( $z_r = 18$  m).

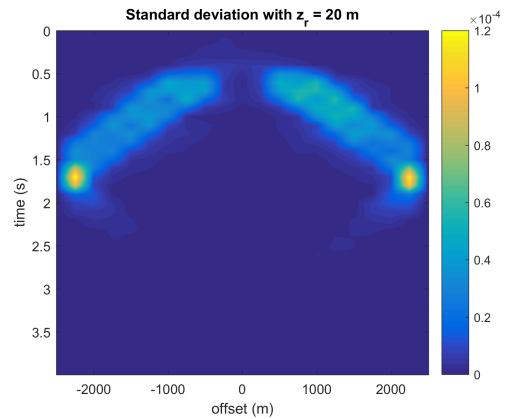


**Figure 4-6:** Standard deviation correct effective receiver depth ( $z_r = 20$  m).

When using a wrong receiver depth of 18 m, the standard deviation result clearly indicates a high inaccuracy around the apex of the hyperbola (bright yellow region in figure 4-5). The standard deviation of the correct receiver depth result (figure 4-6) displays the opposite result; a low standard deviation around the apex, which implies a high accuracy. For both cases the standard deviation is high at the tails of the hyperbola, implying an increase of inaccuracy of the method at these areas.

Figure 4-7 displays the standard deviation of the effective water surface reflectivity. A similar result is observed as the standard deviation result of the effective receiver depth map. The only difference is observed near the area where the arrow is pointing. This area in the standard deviation figure can be traced back to the effective water surface reflectivity map (LHS figure 4-4). It is observed that the estimate is around -0.9 (light blue), whereas the estimate of the first event is normally -1 (dark blue). This indicates that the AED method is more error prone to the variability of water surface reflectivity than receiver depth.

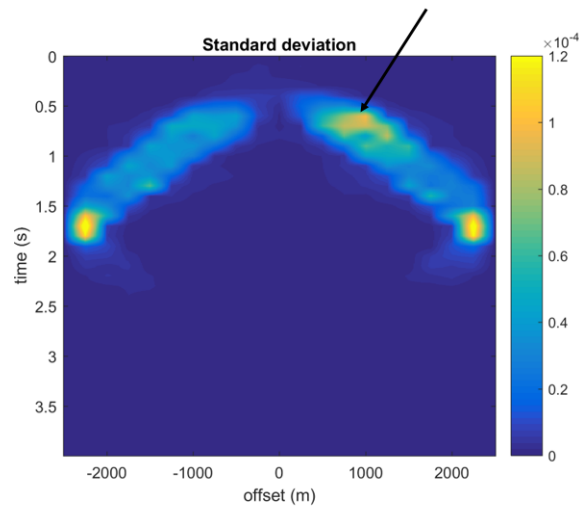


**Figure 4-7:** Standard deviation effective water surface reflectivity, tested with  $r_c = -1, -0.99, \dots, -0.7$ .

The result from the standard deviation calculations allows the user to evaluate the quality of the values obtained in the effective depth and effective water surface reflectivity maps. The standard deviation results of the effective receiver depth and effective water surface reflectivity show great similarity. The uncertainty clearly increases the further away we are from the apex and therefore those values and in particular the values at the edges should be considered to be less reliable. To explain why the standard deviation values around the apex are so low (high accuracy), we must consider the residuals around this region. A low standard deviation indicates that the values of the residuals are similar, if not the same. A window that is placed over the top of the apex will contain residuals that are aligned symmetrically. If the residuals on both top sides of the hyperbola are similar, the resulting spread of values should be small i.e. a low standard deviation. Sliding the window down to a side of the hyperbola will contain some matching residuals on the hyperbola but also contain residuals that fall outside the event. The a-symmetric distribution of the residuals results in a higher spread of values i.e. a high standard deviation.

## 4-5 Test case 1: Two different receiver depths

To determine whether the AED method can detect a change of receiver depth for different events, the method is tested on a new dataset with similar parameter settings as the previous example. The only changes are an increased offset (-5000m to 5000 m) and two events recorded at different depths 22 m (first event) and 18 m (second event) depth. The receiver depths tested now range from 16 m to 24 m (again in steps of 0.02 m) to allow the method to compare numerous minimum residuals. Figure 4-8 displays the results.

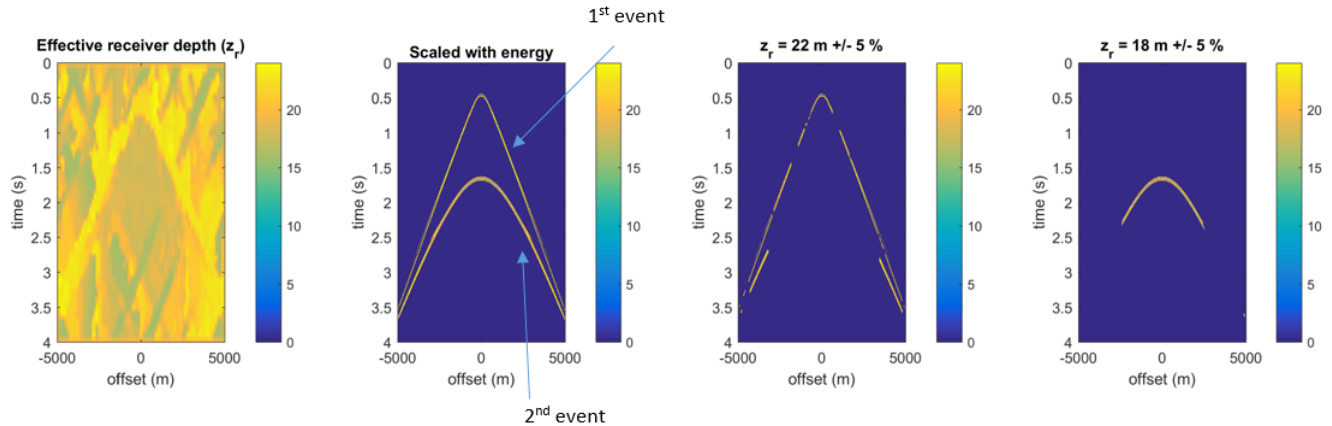


**Figure 4-8:** Obtaining varied receiver depth, first event receiver depth at 22 m and second at 18 m. Window size of 51x51.

The figure on the LHS clearly indicates a receiver depth around 22 m (yellow color) for the first event and a receiver depth around 18 m (light green color) for the second event. The two figures on the right illustrate the areas which obtained 22 m  $\pm$  5% (second RHS figure) and 18 m  $\pm$  5% (RHS figure). The corresponding standard deviation result of the effective receiver depth map can be seen in figure 4-9. The same trend is observed as the earlier standard deviation results: the values around the apex are more accurate than around the tails. The second event does indicate a lower standard deviation at the tails of the hyperbola when compared to the first event. This implies the result of the effective receiver depth of the second event is more accurate over a longer stretch of the event. This observation can be linked to the figure on the RHS (fig. 4-8); there is a good match with the actual receiver depth value of 18 m.

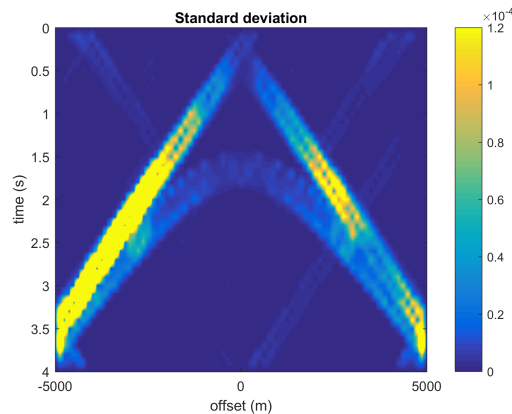


**Figure 4-9:** Standard deviation, first event receiver depth at 22 m and second at 18 m. Window size of 51x51.

It has been shown that the AED method can successfully determine a change of receiver depth for different events (with a 5% error margin). Next, it will be investigated whether this also holds for the water surface reflectivities.

## 4-6 Test case 2: Two different water surface reflectivities

To determine whether the AED method can detect a change in water surface reflectivity for different events, the method is tested on a dataset that contains two events with different water surface reflectivities (-0.9 and -0.95). Both events were recorded with a constant receiver depth of 20 m.

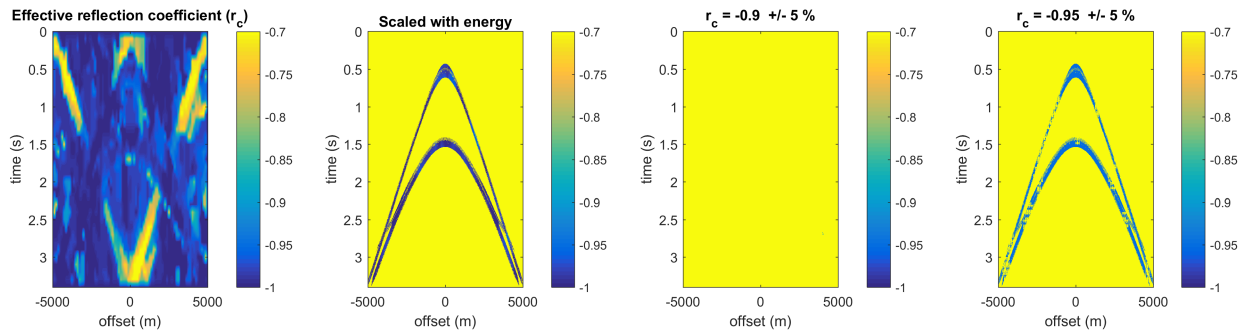


**Figure 4-10:** Obtaining varied water surface reflectivities, first event water surface reflectivity at -0.9 and second at -0.95. Window size of 51x51.

The result from obtaining two different effective water surface reflectivities is reasonable for the second event but not the first (figure 4-10). The -0.95 water surface reflectivity of the second event has been obtained but the -0.9 value is nowhere to be seen. All values are present around -0.95 +/- 5% (displayed in the RHS figure 4-10). The standard deviation result (fig. 4-11) indicates that the tails of the hyperbola are inaccurate, moving towards the apex the inaccuracy slightly decreases but does not improve much. Note that the range for the colorbar has increased, this was necessary because the dataset was modeled in a less rigorous way.

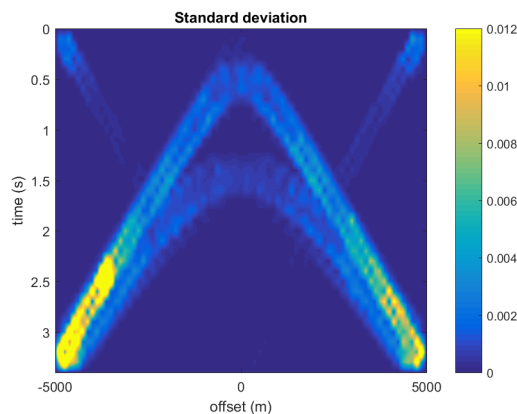


**Figure 4-11:** Standard deviation, varied water surface reflectivities, first event receiver depth at -0.9 and second at -0.95. Window size of 51x51.

From this result, a conclusion can already be drawn that the AED method does not seem to work for plural water surface reflectivities. In the chapter with concluding remarks a link is made with this result and with the earlier sensitivity study in chapter 2.

## 4-7 Test case 3: Unknown water surface reflectivity and receiver depth

The AED algorithm is run on a dataset where the water surface reflectivity and receiver depth were unknown beforehand. The other parameter settings were kept unaltered. Figure 4-12 displays the effective receiver depth result obtained. A first glance at the effective receiver depth map scaled with energy (RHS figure 4-12) shows that the receiver depth increases from negative to positive offset (light orange/green on left towards brighter orange on the right). This gives an indication the dataset was modeled with a slanted streamer cable.

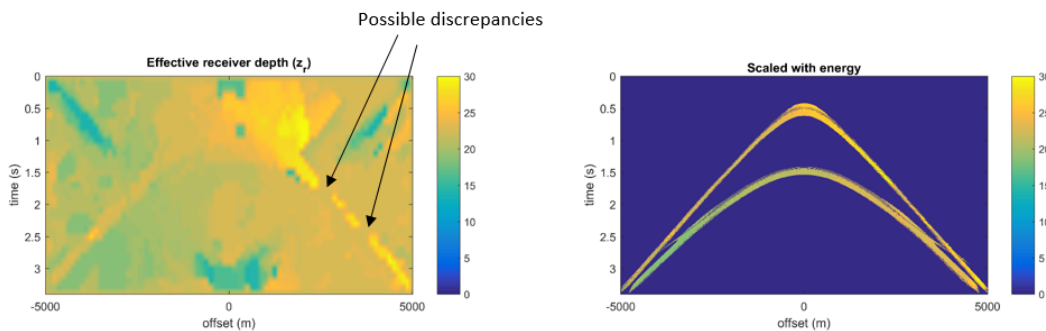


**Figure 4-12:** AED result, tested with receiver depths 14 m - 30 m. Window size 51x51.

The corresponding standard deviation result (fig. 4-13) indicates that the accuracy around the full stretch of the first event is relatively the same. In the second event around the apex, the standard deviation is lower implying the result is more accurate around that area.

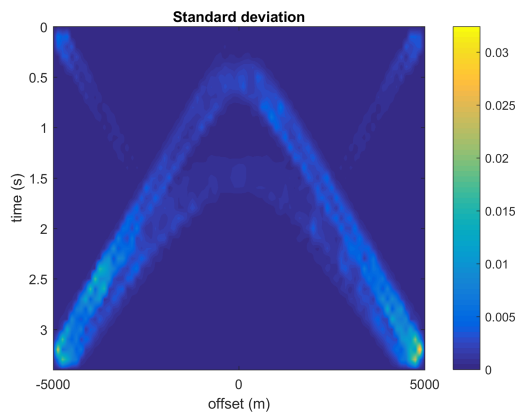


**Figure 4-13:** Standard deviation of AED receiver depth result.

Next, the event tracking method is utilized to give a better representation of the effective parameter results from the events. Considering the window size could result in different outcomes, different window sizes are tested and the effective receiver depth obtained per event is depicted in figures 4-14 and 4-15.

First event

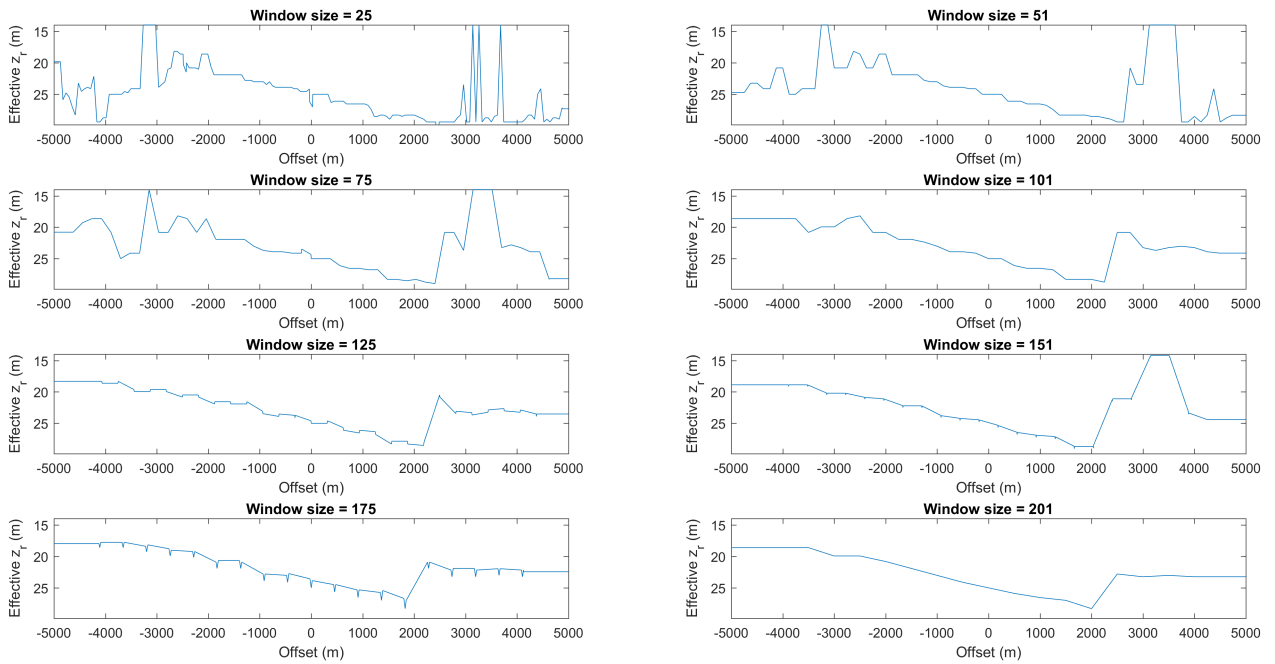


Figure 4-14: First event effective receiver depth.

Second event

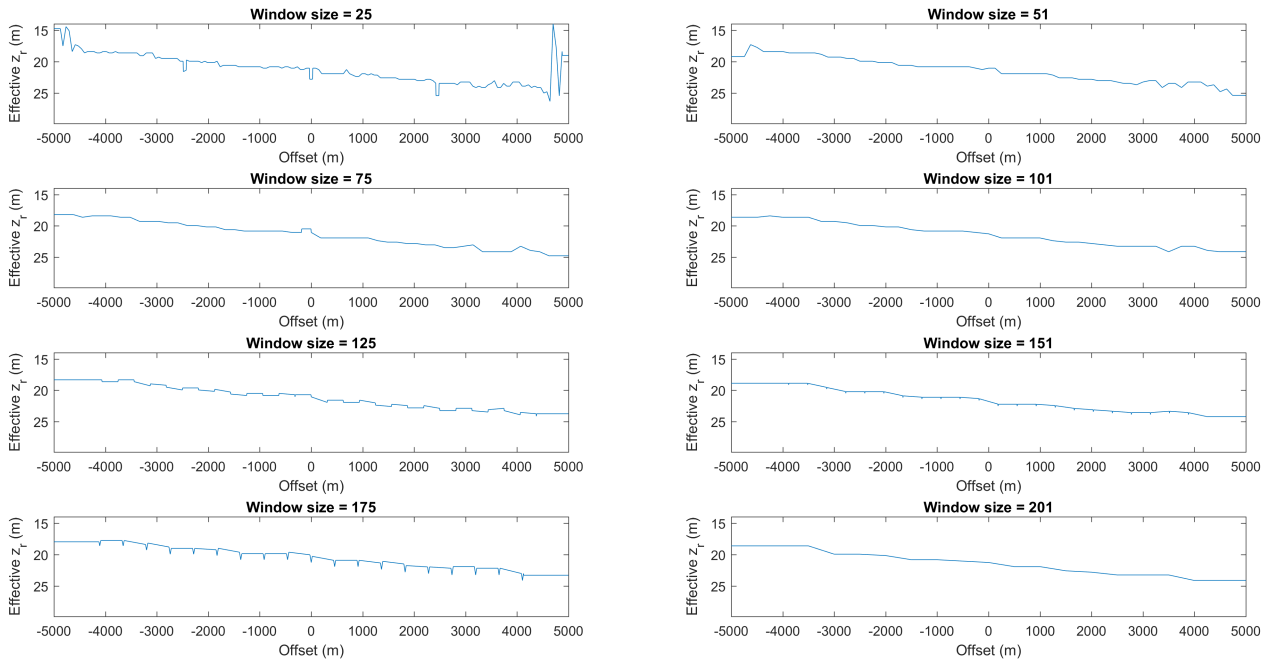


Figure 4-15: Second event effective receiver depth.

Both events show a downward dipping curve from left to right. This indicates the use of a slanted streamer. Increasing the window size displays a smoother dipping line, this favors the use of bigger windows. A disadvantage with the bigger windows is the dipping event flattening out at the sides, this could be a false illustration of reality. Edge effects in the algorithm could be the cause of this problem. The results from the second event look more promising compared to the first event. The first event has a jump in the descending line at an offset around 2000 m. This result can be traced back to figure 4-12 where the first event tends to oscillate from 30 m (yellow) to 20 m (green) (indicated with arrows).

The standard deviation results of the 1st event (figure 4-16) display a sudden jump around offset 2000 m when the largest windows are used (bottom figures 4-16). For the other window sizes this is not the case. No explanation - using the standard deviation result - of the sudden increase of the effective receiver depth at this offset can be made. Possible modeling errors could have been the cause of this. Taking a top-level view of the standard deviations (figures 4-16 and 4-17) it can be observed that the accuracy towards the far offsets (-5000 m and 5000 m) is lower than in the center. This is similar to the result in the earlier 2D standard deviation calculations (figures 4-7 and 4-9).

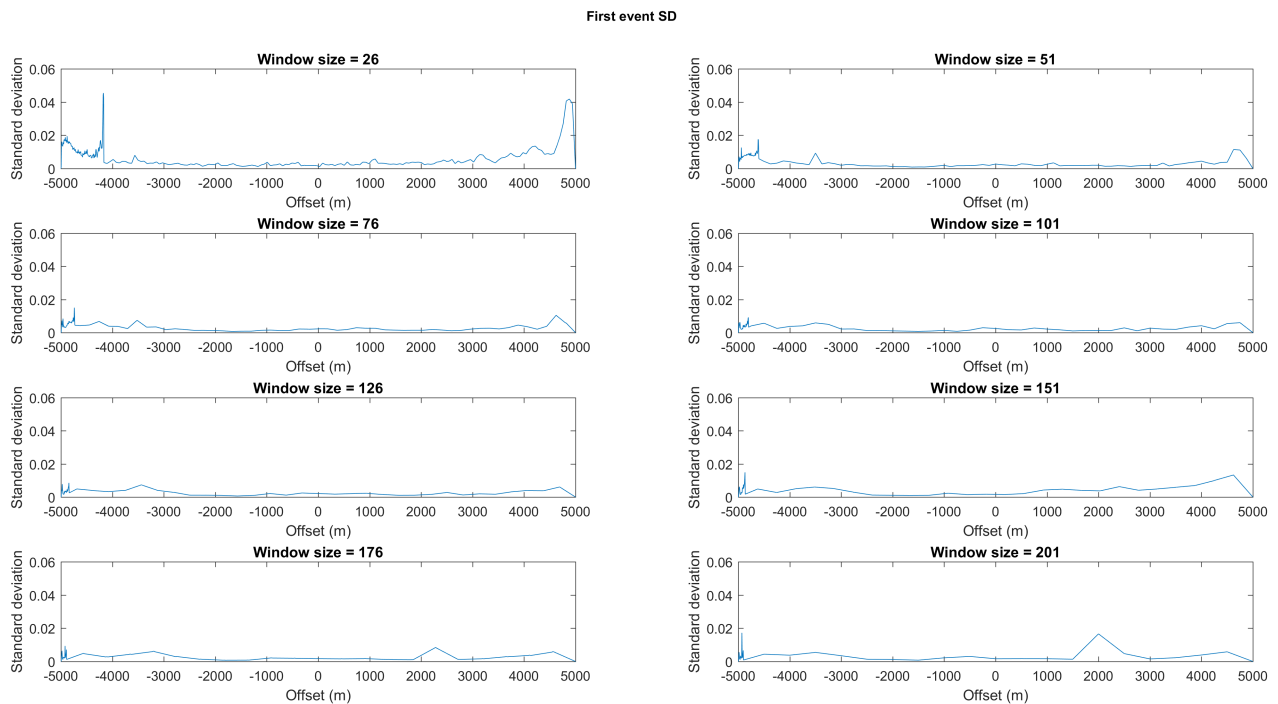


Figure 4-16: 1st event effective receiver depth standard deviation.

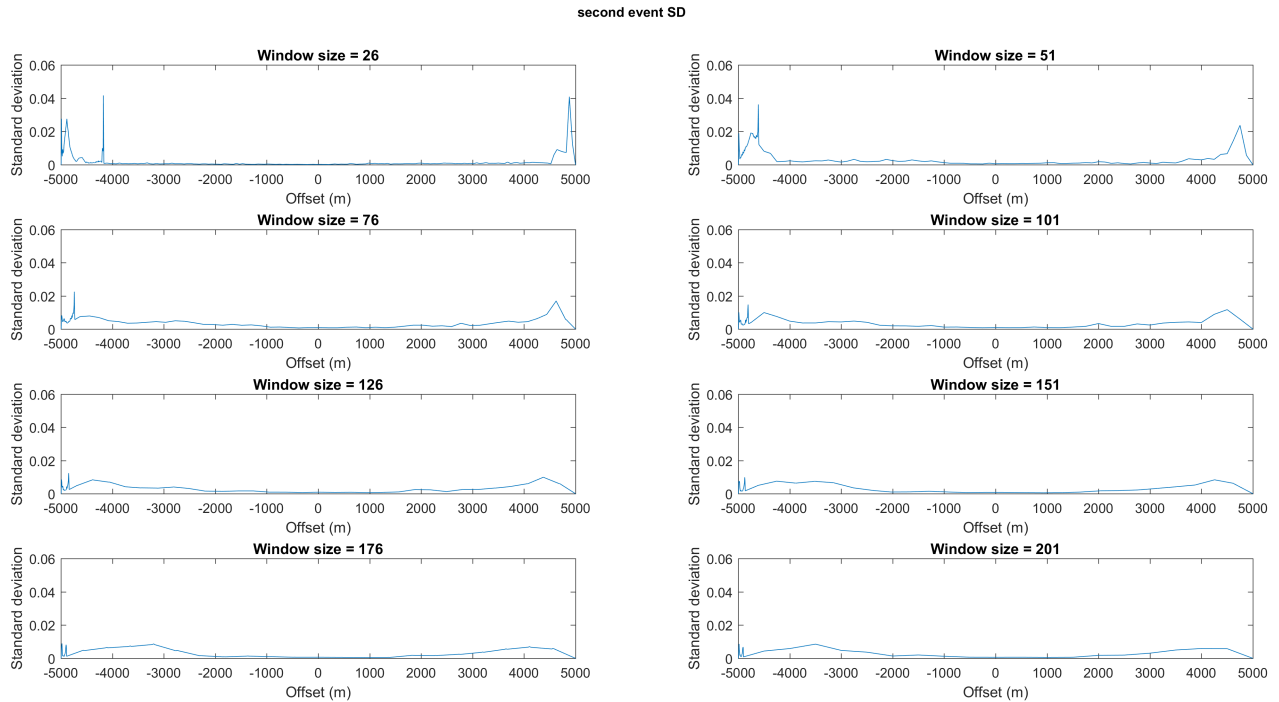


Figure 4-17: 2nd event effective receiver depth standard deviation

### Effective water surface reflectivity

Figure 4-18 displays the result from the AED method on obtaining the water surface reflectivities. At first glance the water surface reflectivities seem to oscillate from -1 to -0.9 (dark blue to light blue).

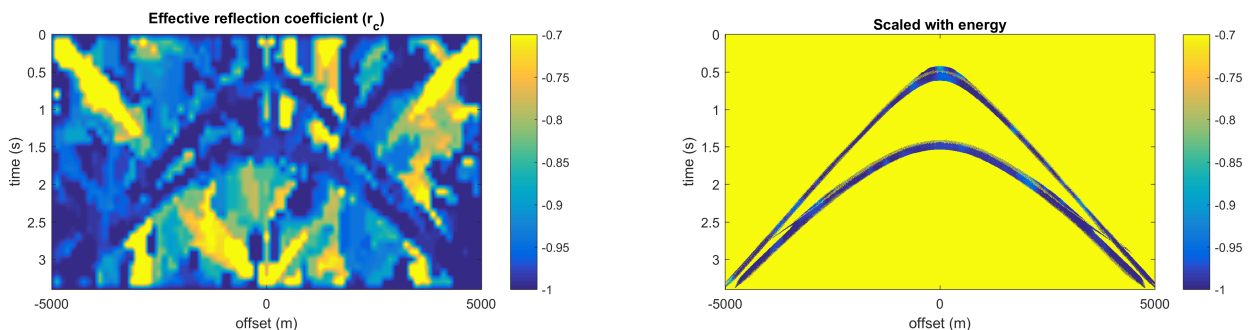
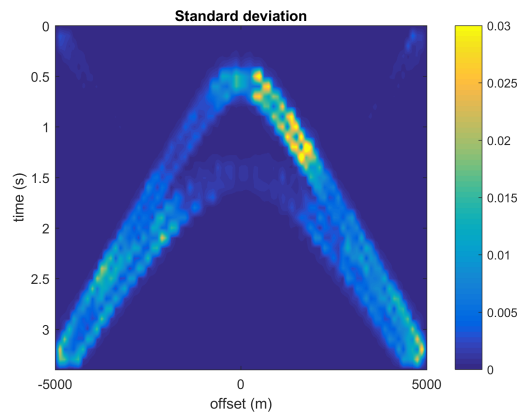


Figure 4-18: AED result, tested with  $r_c = -1, -0.99, \dots, -0.7$ .

The corresponding standard deviation is displayed in figure 4-19.



**Figure 4-19:** Standard deviation effective water surface reflectivities.

Different window sizes are again tested to examine which window size gives the most realistic results in terms of effective water surface reflectivity (figures 4-20 and 4-21). For the first event, the smaller windows (25 - 101) show a similar pattern of a decrease in effective water surface reflectivities from offsets 0 m - 5000 m. A window size of 125 and 175 results in an irregular representation of the water surface reflectivity, a probable cause could be interpolation errors. The larger window (201) result shows some similarity to the results utilizing smaller window sizes, be it a more averaged representation. The actual water surface reflectivity for the first event is hard to deduce from the results utilizing different windows. Possibly, the water surface reflectivity is -1 at negative offsets and increases slightly towards positive offsets. The results when utilizing smaller windows for the second event are again similar. Utilizing larger windows results in interpolation errors (125 and 175) or a flat averaged representation (151 and 201). The effective water surface reflectivity of the second event, based on the results from the smaller windows, seems to oscillate from -1 to -0.95. The larger window (201) indicates the effective water surface reflectivity is on average -1 and only slightly jumps towards -0.96 at an offset of 1500 m - 3000 m.

First event

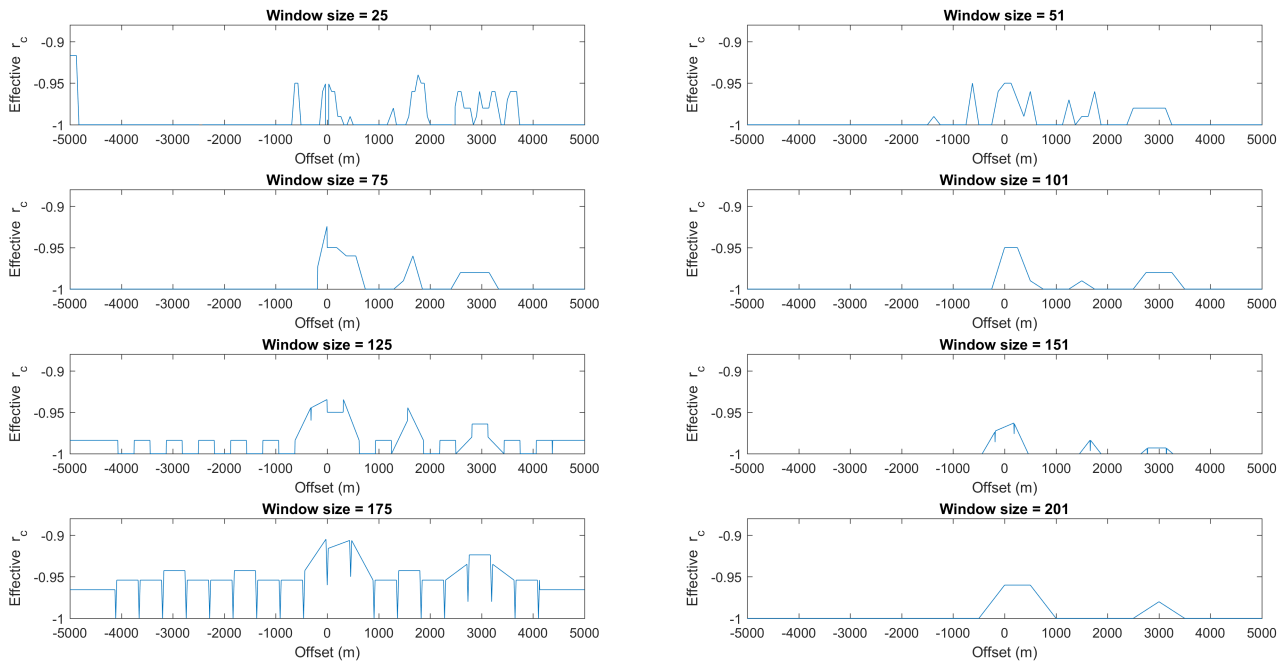


Figure 4-20: 1st event effective water surface reflectivity.

Second event

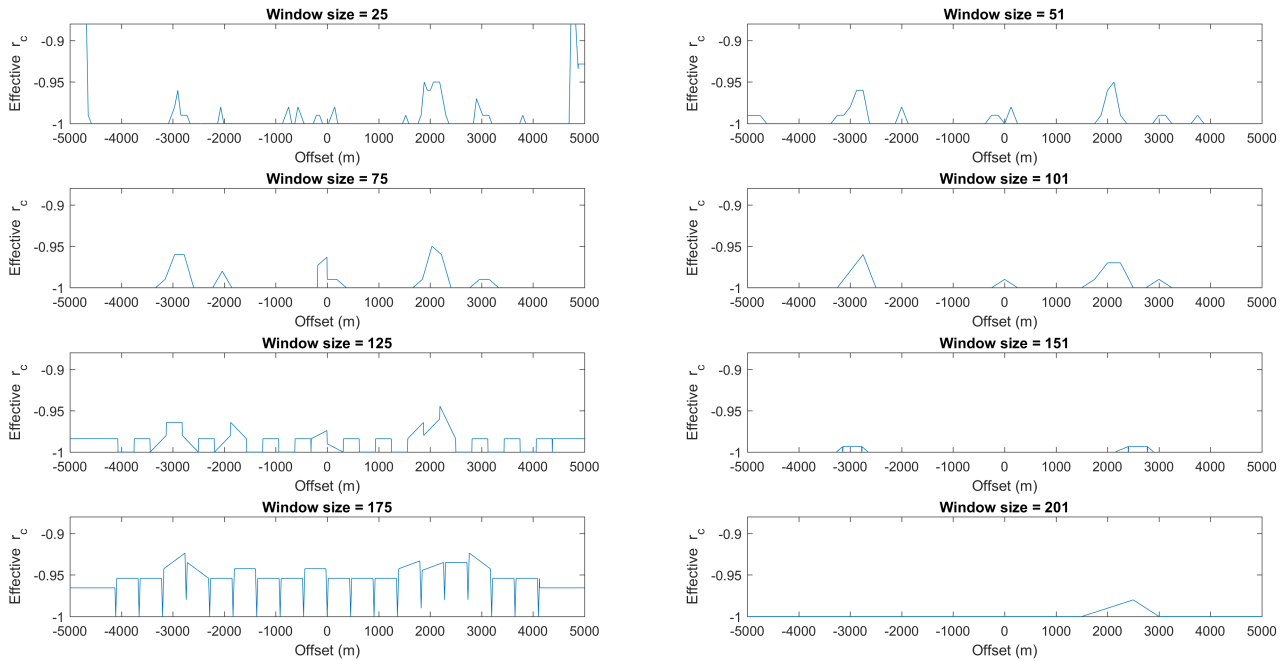


Figure 4-21: 2nd event effective water surface reflectivity.

The corresponding standard deviation figures 4-22 and 4-23, illustrate that the smaller window sizes (25 and 51) result in high standard deviations at the edges. Increasing the window size causes the edge effects to disappear at the right (positive offset) but remain on the left side (negative offsets). A possible explanation could be that the use of a slanted streamer causes the edge effect to be amplified on one side (and reduced on the other) due to the a-symmetry involved. There is also a sudden jump at offset 1000 m in the window size of 25. The best choice seems to use a bigger window considering the irregularities when using smaller windows.

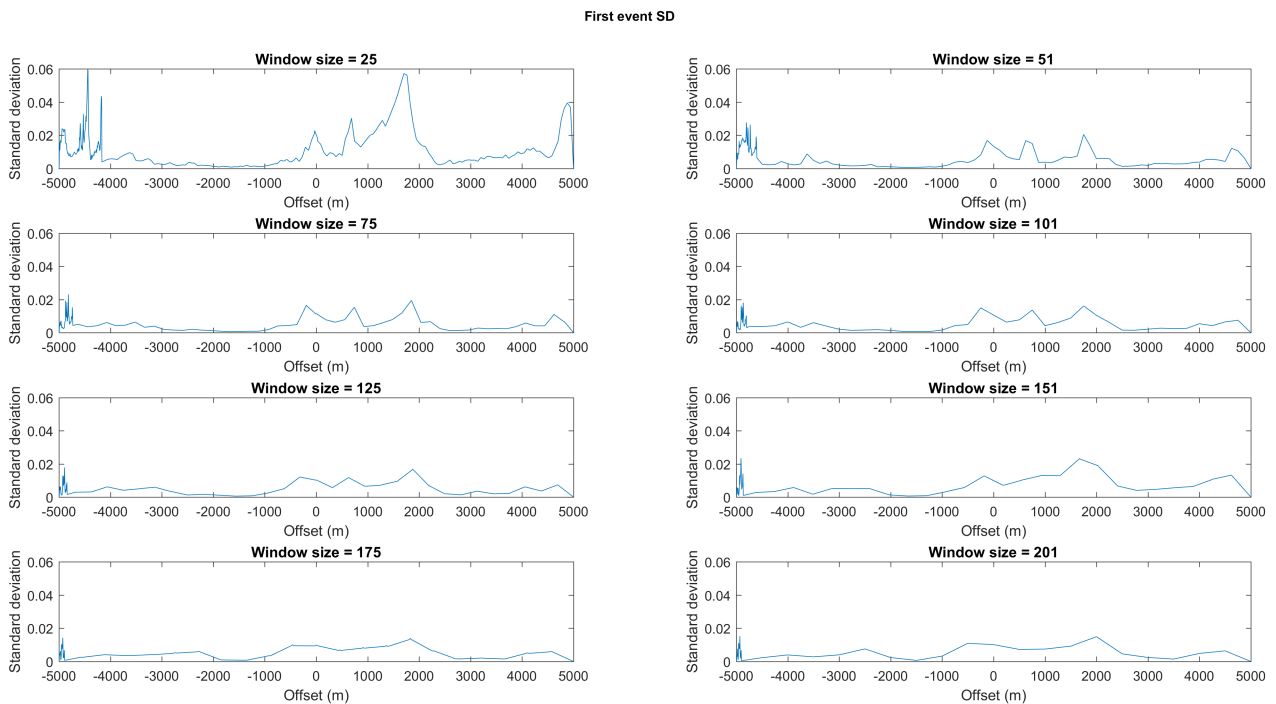
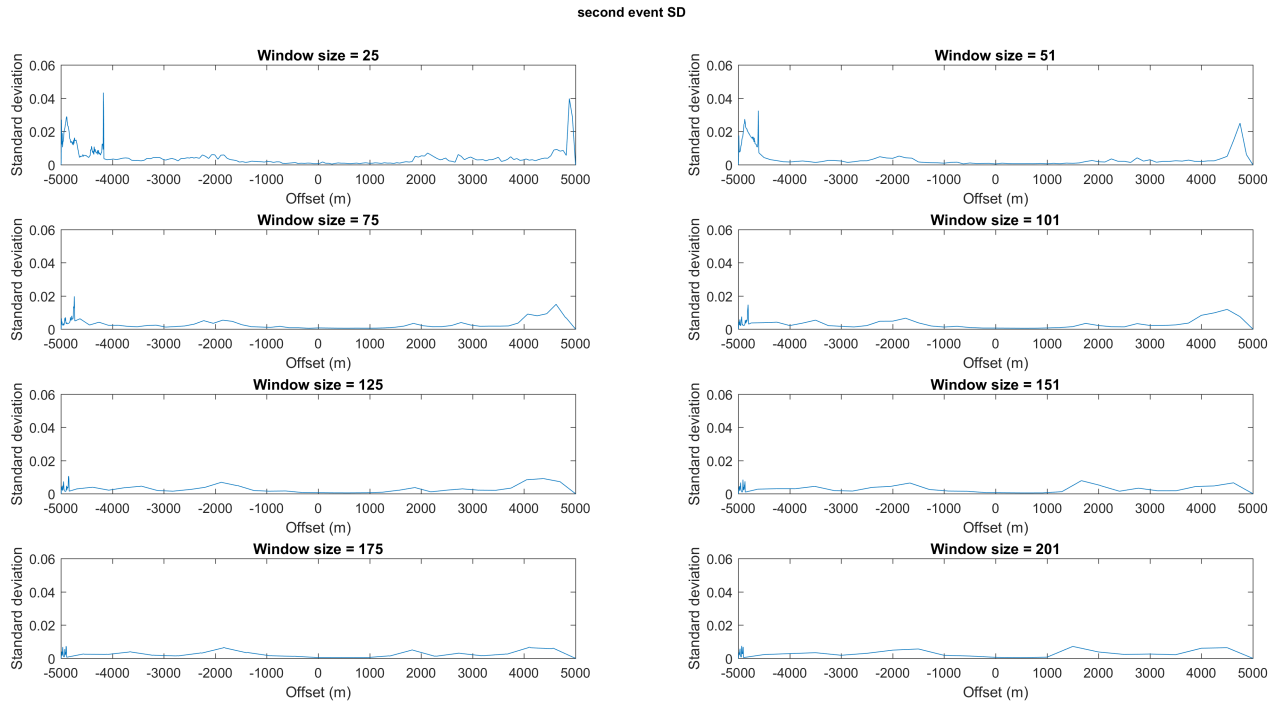


Figure 4-22: 1st event effective water surface reflectivity standard deviation.



**Figure 4-23:** 2nd event effective water surface reflectivity standard deviation.

After testing the AED method to search for the unknown water surface reflectivity and receiver depth, the modeling parameters were revealed. The first event was modeled for a slanted streamer going linearly from 15 m at - 5000 m offset to 35 m at 5000 m offset. The reflectivity also changed linearly from -1 to -0.98, respectively. The second event used a reduced slant from 18 m to 25 m, and the reflectivity decreased from -0.96 to -1.

Utilizing the event following method to deduce the effective receiver depth, resulted in a representation of a downward sloping streamer for both events. The first event resulted in a strange jump around the 2000 m offset area, after discussion it became evident this could be the result of modeling errors. The far offsets did not retrieve the modeled receiver depths. Considering edge effects were not taken into account properly, it can be deduced that when extrapolating the slanted streamer - at the point it becomes horizontal - towards the edges, the expected receiver depths are obtained. The expected water surface reflectivity was only slightly visible for the first event when utilizing small windows; at negative offsets there was a -1 water surface reflectivity and towards positive offsets the values sometimes decreased to -0.95. Some of the results utilizing larger windows were prone to interpolation errors. The effective water surface reflectivity results of the second event when utilizing different windows, did not match with the modeled values. The corresponding standard deviation results did not justify the irregularities observed. It can be concluded that obtaining variable water surface reflectivities in the case of a variable receiver depth is a challenging task for the AED method.

The results from the adaptive echo-deblending algorithm are promising for acquiring the receiver depth but less promising for the water surface reflectivity. The water surface reflectivity is probably best estimated when the receiver depth is known exactly. A large window size

(e.g. 201x201) should be utilized when running the AED method considering it takes care of outliers and the standard deviation result is low on average.

The single event tracking capability is at a preliminary stage. It should be improved to remove edge effects and to ensure every window interpolates the effective parameter values properly. In the next chapter final conclusions will be drawn and recommendations for future work will be given.

# Conclusion and Recommendations

Traditional deghosting works under specific ideal circumstances. However, in a dynamic environment the assumptions are not met for an ideal case of deghosting. Numerous methods exist that attempt to resolve uncertainties like unknown receiver depths due to rough seas, unknown water surface reflectivities and variable acoustic wave velocities in water. However, a proper uncertainty analysis is missing in these methods. In this thesis, a new adaptive deghosting method is introduced that includes an uncertainty analysis.

A sensitivity analysis on relevant parameter settings of conventional deghosting has shown that a percentage wise change in the acoustic wave velocity in water causes the greatest disturbance in results. A similar change in the receiver depth also causes a high disturbance whilst such a change in water surface reflectivity seems to have the least effect on the deghosting result.

A recently introduced deghosting method called echo-deblending was extended into an adaptive windowing based deghosting method (AED). The main reason for using echo-deblending in an adaptive method is that it is straight forward to implement an uncertainty analysis. Besides the adaptive windowing based retrieval of parameter values, the uncertainty of the determined values of the receiver depth and water surface reflectivity can be quantified through the use of a standard deviation calculation. The echo-deblending method uses an iteration based thresholding scheme in the t-x domain. The use of this domain also provides the AED method the ability to track only specific events of interest, which can be of particular importance in low signal-to-noise ratio datasets, while it also reduces runtime. The information obtained for those events can be very valuable for later processing methods.

The results from the AED method on obtaining the receiver depth look promising on synthetic data sets with single and dual hyperbolic events. The uncertainty analysis on the corresponding hyperbolic events indicated a high certainty around the apex but increasing uncertainty towards the tails. This effect could be explained due to the symmetry of the residuals in a window around the apex and a-symmetry at the tails. The effective water surface reflectivity results were promising for an initial synthetic dataset. The AED method gave a sub-optimal result for a shallow event in a dataset with two events and different water

surface reflectivities. This could be linked to the earlier result of the sensitivity analysis. The AED algorithm is based on comparing the differences between deghosted results with different parameter settings. The sensitivity analysis indicated that the water surface reflectivity is the least sensitive parameter, which goes some way towards explaining why the AED method did not successfully retrieve the desired water surface reflectivities for shallow events.

The effect of the size of the window for the event tracking method was investigated. Windowing is an important controlling factor where the size determines the amount of smoothing (large windows) vs accuracy (small windows). A large window size resulted in a smooth representation of a slanted streamer on a synthetic dataset. The standard deviations of the larger windows were correspondingly lower as well. The results displayed some edge effects so this could still be improved by future researchers.

What follows is a list of possible improvements of the AED method and items for additional research.

- Testing the AED method on different acoustic wave velocities in water.
- Investigating more realistic synthetic datasets that try to incorporate circumstances like e.g. a rough sea.
- The water surface reflectivity is known to vary with incidence angle and frequency. The AED method could be extended in this area.
- Extending the method to determine the receiver depth and water surface reflectivity simultaneously.
- Test the algorithm on real data.
- Investigate methods to determine an optimal window size.
- Any edge effects could be reduced by some improved form of stabilized extrapolation.
- Constraints must be built in that ensure the obtained values remain stable.
- Currently the windows contribute in equal measure to the overlap but this could be changed to some form of a weighted summation which accounts for the uncertainty derived from the standard deviation results.
- The echo-deblending algorithm by itself can handle noise. Perhaps the AED algorithm can use this capability to its advantage.
- Use the outcome of AED to improve deghosting methods

To conclude, we have shown that a dynamic environment around seismic acquisition necessitates to adaptively locate the correct parameter settings and quantify the uncertainty of these values. Furthermore, this thesis has laid the foundations for future research to apply the method on real data to obtain the actual deghosting result.

---

# Bibliography

- [wik, 2010] (2010). Offshore marine seismic surveying. <http://wikigrewal.com/offshore-marine-seismic-surveying/>. Accessed: 2017-04-10.
- [BP, 2016] (2016). Sources of energy, now and in the future. <http://www.bp.com/en/global/corporate/energy-economics.html>. Accessed: 2017-03-19.
- [IEA, 2016] (2016). World energy outlook. <http://www.iea.org/newsroom/news/2016/november/world-energy-outlook-2016.html>. Accessed: 2017-03-20.
- [Aharchaou and Anderson, 2016] Aharchaou, M. and Anderson, J. E. (2016). Adaptive receiver de-ghosting for deep-tow pressure data. *86th SEG Annual International Meeting*.
- [Barret et al., 1994] Barret, R., Berry, M., Chan, T. F., Demmel, J., Donato, J., Dongarra, J., Eijkhout, V., Pozo, R., Romine, C., and van der Vorst, H. (1994). *Templates for the Solution of Linear Systems: Building Blocks for Iterative Methods*. SIAM.
- [Beasley et al., 2013] Beasley, C., Coates, R., and Ji, Y. (2013). Wave equation receiver deghosting. *75th EAGE Conference and Exhibition*.
- [Berkhout and Blacquiere, 2015] Berkhout, G. and Blacquiere, G. (2015). Deghosting by echo-deblending. *77th EAGE Conference and Exhibition*.
- [Carlson et al., 2007] Carlson, D., Long, W., Tobti, H., Tengehamn, R., and Lunde, N. (2007). Increased resolution and penetration from a towed dual-sensor streamer. *First Break*, (25):71–77.
- [Ferber and Beasley, 2014] Ferber and Beasley (2014). Adaptive receiver de-ghosting for deep-tow pressure data. *76th EAGE Conference and Exhibition*.
- [Fokkema and van den Berg, 1993] Fokkema, J. and van den Berg, P. (1993). *Seismic Applications of Acoustic Reciprocity*. Elsevier.
- [Grion et al., 2015] Grion, S., Telling, R., and Barnes, J. (2015). Adaptive de-ghosting by kurtosis maximisation. *77th EAGE Conference Exhibition 2015*.

- [King and Poole, 2015] King, S. and Poole, G. (2015). Hydrophone-only receiver deghosting using a variable sea surface datum. *85th SEG Annual International Meeting*.
- [Kragh et al., 2002] Kragh, E., Laws, R., and Combee, L. (2002). Sea surface shape derivation above the seismic streamer. *64th EAGE Conference and Exhibition*.
- [Liang et al., 2008] Liang, Z., Wei, J., Zhao, J., Liu, H., Li, B., Shen, J., , and Zheng, C. (2008). The statistical meaning of kurtosis and its new application to identification of persons based on seismic signals. *Sensors (Basel)*, 8(8):5106–5119.
- [Moldoveanu et al., 2006] Moldoveanu, N., Combee, L., and Egan, M. (2006). Over/under towedstreamer acquisition: A method to extend the seismic bandwidth to both, higher and lower frequencies. *SEG Technical Program Expanded Abstracts 2006*.
- [Orji et al., 2013] Orji, O. C., Sollner, W., and UiO, L. J. G. (2013). Sea surface reflection coefficient estimation. *83rd SEG Annual International Meeting*.
- [Parkes and Hegna, 2011] Parkes, G. and Hegna, S. (2011). A marine seismic acquisition system that provides a full ghost-free solution. *81st SEG Annual International Meeting*, pages 37–41.
- [Poole, 2013] Poole, G. (2013). Pre-migration receiver de-ghosting and re-datuming for variable depth streamer data. *83rd Annual SEG Meeting Expanded Abstracts*, pages 4216–4220.
- [Rickett et al., 2014] Rickett, J., van Manen, D., Loganathan, P., and Seymour, N. (2014). Slanted-streamer data-adaptive deghosting with local plane waves. *76th EAGE Conference and Exhibition*.
- [Riyanti et al., 2008] Riyanti, C. D., van Borselen, R. G., van den Berg, P. M., and Fokkema, J. T. (2008). Pressure wave-field deghosting for non-horizontal streamers. *SEG Las Vegas annual meeting*.
- [Schuberth, 2015] Schuberth, M. G. (2015). Adaptive deghosting of seismic data a power-minimization approach. diploma thesis, ETH Zurich.
- [Soubaras, 2010] Soubaras, R. (2010). Deghosting by joint deconvolution of a migration and a mirror migration. *80th SEG Annual International Meeting*.
- [Vassalo et al., 2012] Vassalo, M., Eggenberger, K., van Manen, D., zdemir J.O.A. Robertsson, K., and zbek, A. (2012). Reconstruction of the subsurface reflected wavefield on a dense grid from multicomponent streamer data. *74th EAGE Conference and Exhibition*.
- [Wang et al., 2013] Wang, P., Ray, S., Peng, C., Li, Y., and Poole, G. (2013). Premigration deghosting for marine streamer data using a bootstrap approach in tau-p domain. *75th EAGE Conference and Exhibition*.
- [Wapenaar and Berkhout, 1989] Wapenaar, K. and Berkhout, G. (1989). *Elastic wavefield propagation*. Elsevier.
- [Wong et al., 1995] Wong, K, G. S., Zhu, and Shi-ming (1995). Speed of sound in seawater as a function of salinity, temperature, and pressure. *The Journal of the Acoustical Society of America*, (97).

- 
- [Yoo et al., 2017] Yoo, J., Hegge, R., and van Borselen, R. (2017). Deghosting through notches using echo deblending - synthetic and field data examples. *79th EAGE Conference and Exhibition*.
- [Zhang et al., 2016] Zhang, Z., Wu, Z., Wang, B., and Ji, J. (2016). Adaptive windowed deghosting - applications to fаз acquisition. *2016 TGS-NOPEC Geophysical Company ASA*.



---

# Appendix A

---

## Appendices

### A-1 The L1 and L2 norms versus Kurtosis

The  $L_1$  norm is defined as:

$$S = \sum_{i=1}^n |y_i - f(x_i)|, \quad (\text{A-1})$$

where  $y_i$  could refer to the energy of the recorded data  $P_{data}$  and  $f(x_i)$  the energy of a proposed model that should fit the data. The idea would consist of finding the minimum by adapting the model to fit the data.

The  $L_2$  norm is defined as:

$$S = \sum_{i=1}^n (y_i - f(x_i))^2. \quad (\text{A-2})$$

The  $L_2$  norm is also called least squares and it basically minimizes the square of the differences. The difference between the  $L_1$  and  $L_2$  norm lies in aspects such as robustness ( $L_1 > L_2$ ), stability of the solution ( $L_1 < L_2$ ), sparseness of the output ( $L_1 > L_2$ ), and possibility of multiple solutions ( $L_1 > L_2$ ).

Kurtosis is defined as:

$$\frac{\sum_{i=1}^N (Y_i - \bar{Y})^4 / N}{\sigma^4}, \quad (\text{A-3})$$

where  $Y_i$  is a variable at point  $i$  (e.g. autocorrelation),  $\bar{Y}$  the mean of the data,  $\sigma$  is the standard deviation and  $N$  is the number of data points. Kurtosis is a statistical measure that's used to describe the distribution, or skewness, of observed data around the mean.

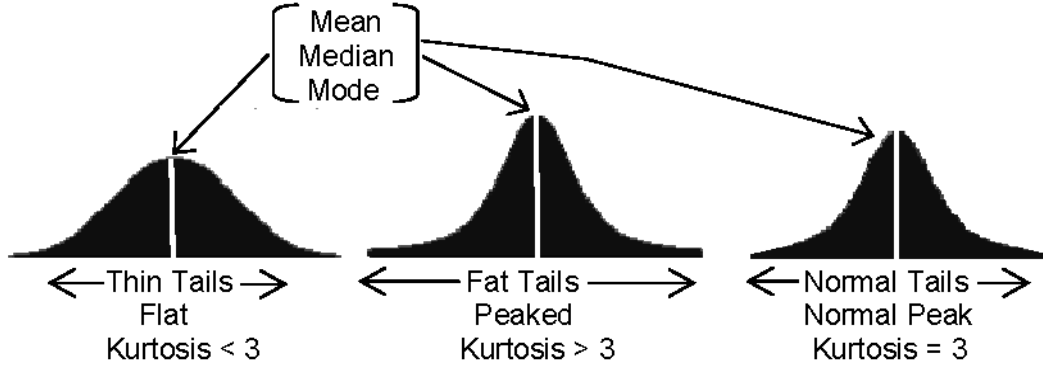


**Figure A-1:** Example of low (LHS figure), high (middle figure) and middle (RHS figure) kurtosis. Figure from [Liang et al., 2008].

A high Kurtosis value indicates a high possibility of a non-Gaussian variable (e.g. autocorrelation) around a mean (middle figure A-1). So when searching for delay-times or reflection coefficients, a high Kurtosis value indicates the most probable delay-time.

## A-2 Direct inversion-based deghosting

In this appendix, applications of direct inversion-based deghosting operators are discussed, based on the 1D and 2D equivalents of the deghosting equation.

### A-2-1 1-D deghosting

In the most ideal situation of deghosting, we only have the primary upgoing wavefield and its secondary downgoing ghost wavefield. In the 1D case this can be modeled with two Dirac delta functions. The primary upgoing wavefield occurs at time zero, indicating the time the upgoing primary wavefield enters the receiver. The second Dirac delta function occurs at a delay ( $t_{\Delta}$ ) that represents the time the downgoing ghost wavefield arrives at the receiver. The Dirac delta function represents an ideal impulse response from the seismic source. The zero pressure zone above the sea surface will result in a sign change of the delayed Dirac delta function (eq. A-4).

$$\delta(t) - \delta(t - t_{\Delta}). \quad (\text{A-4})$$

When we apply a convolution of these time based signals with an arbitrary upgoing wavefield, the result is the recorded data at the receiver:

$$p_{data}(t) = [\delta(t) - \delta(t - t_{\Delta})] * p^{up}(t), \quad (\text{A-5})$$

where  $p_{data}(t)$  is the data containing the ghost, and  $p^{up}(t)$  is the primary upgoing wavefield. Applying a Fourier transformation of the signals in the time domain (eq. A-5) will cause the convolution to become a multiplication in the frequency domain (eq. A-6):

$$\hat{p}_{data}(f) = \hat{g}(f)\hat{p}^{up}(f), \quad (\text{A-6})$$

where  $\hat{g}(f)$  is the ghost operator and is expressed as:

$$\hat{g}(f) = 1 - e^{-j2\pi ft_{\Delta}}. \quad (\text{A-7})$$

The frequency spectrum of the ghost operator is shown in figure A-2.

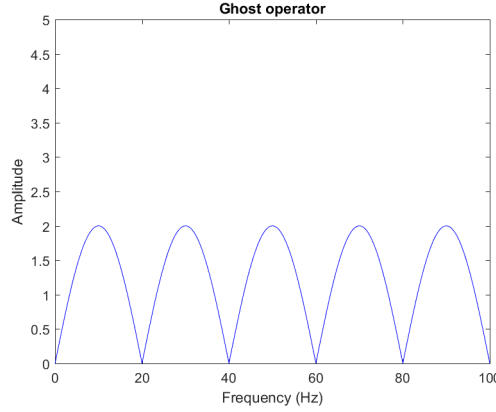


**Figure A-2:** Frequency spectrum of ghost operator.

The earlier figure that was presented (fig. 2-3) illustrates a primary upgoing wave and a ghost with a slight time delay ( $t_{\Delta} = 0.05$  s). The frequency spectra from the primary and ghost wavefields are clean lobes but once combined show notches at periodic intervals (0,20,40,60 Hz). These notches can be predicted by inverting the time shift ( $\frac{1}{0.05} \cdot [0, 1, 2, \dots = 0, 20, 40, \dots, 20 \cdot n$  Hz), where  $n \in \mathbb{N}$ .

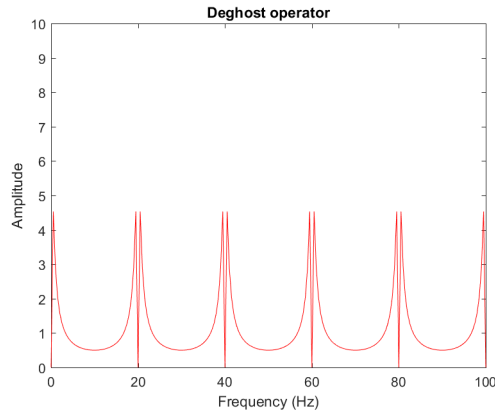
The simplest deghosting method comes in the form of an inverse filter, where the ghost operator is inverted and applied to the data and hence will act as a filter (eq. A-8):

$$\frac{\hat{P}_{data}(f)}{\hat{g}(f)} = \hat{p}^{up}(f). \quad (\text{A-8})$$

This method is very rudimentary. The denominator ( $\frac{1}{(1 - e^{-j2\pi ft_{\Delta}})}$ ) will become zero at the periodic intervals 0,20,40,60 Hz, causing a singularity. The denominator and numerator are multiplied by the complex conjugate of the ghost operator to ensure the phase is preserved (phase becomes zero when a signal is multiplied by its complex conjugate) (eq. A-9). Additionally, some stabilization ( $\lambda = 0.01$ ) is added in the denominator to overcome the singularity. The deghosting operator can now be expressed as:

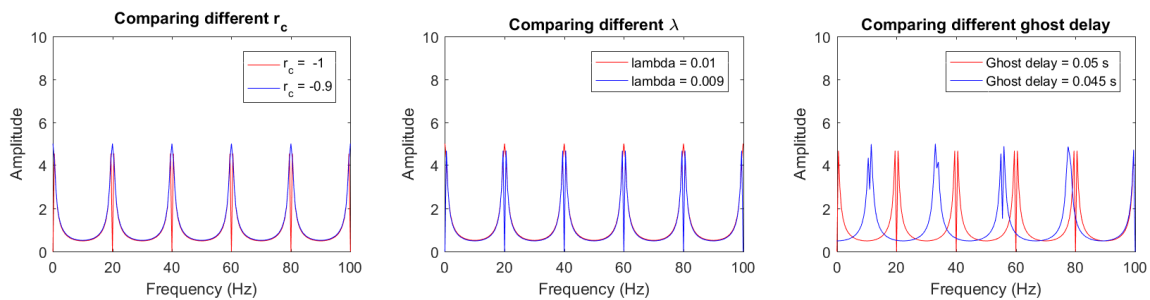
$$\hat{g}_{degh}(f) = \frac{\hat{g}^*(f)}{\hat{g}(f)\hat{g}^*(f) + \lambda}. \quad (\text{A-9})$$

Figure A-3 illustrates how the deghosting operator works. It basically compensates for the lost frequencies at the notches, the sharp edges at the notches of the deghosting operator indicate the short comings of the technique.



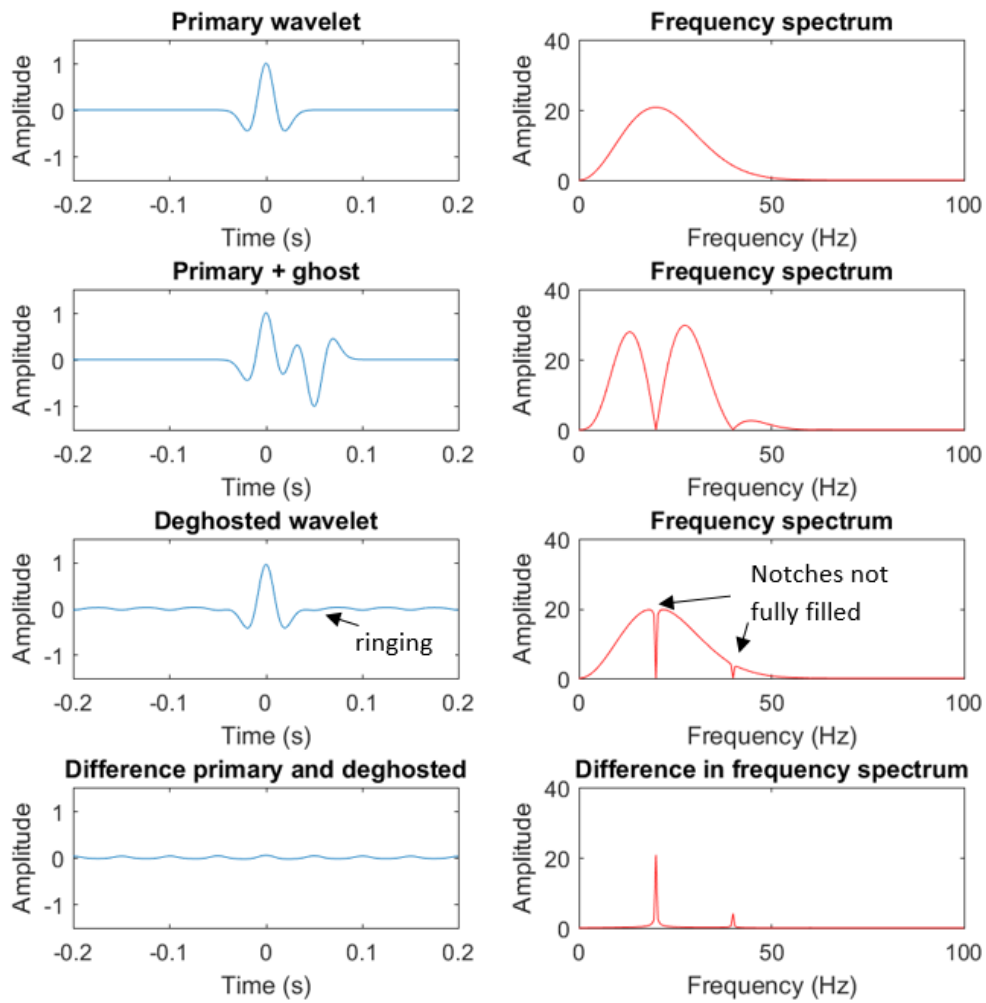
**Figure A-3:** Frequency spectrum of deghosting operator.

Figure A-4 illustrates how varying the values for the different deghosting parameters (water surface reflectivity, stabilization factor, ghost delay) has an effect on the shape of the deghosting operator. Clearly, varying the ghost delay (which is related to acoustic wave velocity in water and receiver depth, according to  $t = \frac{c}{2x_3}$ ) has the greatest influence on the shape of the deghosting operator.



**Figure A-4:** Comparing change in deghosting operator as parameters are varied.

In fig. A-5, an illustration of the inverse filtering technique is presented. It can be observed (middle RHS figure) how adding the ghost destroys the amplitude at certain frequencies (20, 40, 60 Hz) and increases the amplitudes in between these frequencies (i.e., the locations of destructive and constructive interference). The deterministic deghosting result (second from bottom RHS figure) shows a recovery of the amplitudes except at the notches.



**Figure A-5:** Time (LHS) and frequency (RHS) amplitude plots of primary (top) wavefield, primary + ghost (second row), deghosted result (third row) and the difference in primary and deghosted (bottom).

Increasing the stabilization factor ( $\lambda$ ) from 0.01 to 0.1 will cause an increase in ringing which can be seen in figure A-6. The increase in stabilization factor also reduces the high amplitude frequency compensation around the notches.

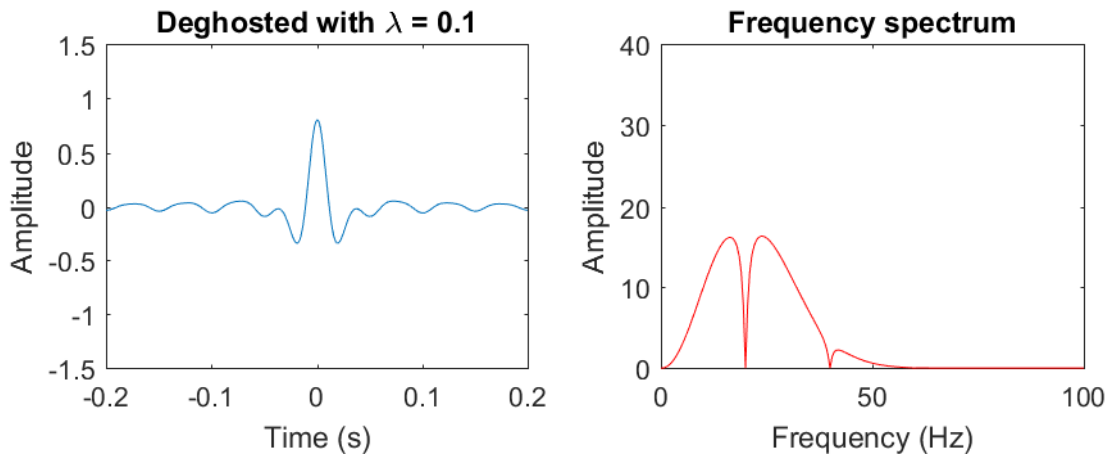


**Figure A-6:** Deghosted result with a stabilization factor  $\lambda = 0.1$ .

### A-2-2 2-D deghosting

If we now take a look at 2D (time-space) deghosting we can take the direction of propagation into consideration. This is more realistic because pressure waves will travel in all directions when shot from an air gun. Including the direction of propagation leads to:

$$x_3^R = \frac{ct}{2} \cos(\theta), \quad (\text{A-10})$$

where theta ( $\theta$ ) is the angle between the incoming signal at the receiver and the vertical (fig. A-7).

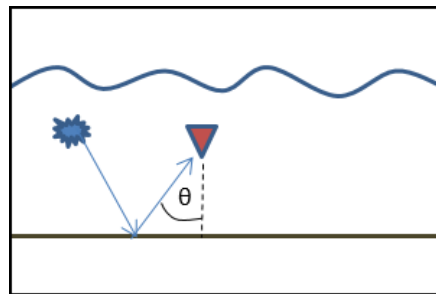


**Figure A-7:** Wave propagating at an angle.

After 2-D acquisition the data will be in the time-space ( $t - x$ ) domain where it can be transformed to either the frequency-wavenumber ( $f - k$ ) or frequency-slowness ( $f - p$ ) domains. Wavenumber ( $k$ ) is the spatial frequency of a wave expressed in radians per unit distance. It can be seen as the number of waves that exist over a specified distance (the distance between receivers), this is analogous to frequency being the number of cycles per unit time.

The 2D equation of the convolution of a ghost operator and an arbitrary upgoing

wavefield in the frequency-wavenumber domain can be expressed as:

$$P_{data}(f, k_1) = G(f, k_1)P^{up}(f, k_1), \quad (\text{A-11})$$

where the ghost operator is:

$$G(f, k_1) = 1 + r_c e^{-j2k_3 x_3^R}, \quad (\text{A-12})$$

and where the vertical wavenumber is expressed as  $k_3 = \sqrt{((\frac{2\pi f}{c})^2 - k_1^2)}$ . The reflection coefficient of the sea surface ( $r_c$ ) is assumed to be constant at -1 and the propagation velocity in water ( $c$ ) homogeneous at 1500 m/s. The horizontal wavenumber ( $k_1$ ) is calculated from the data ( $\frac{2\pi}{dx}$ ), where  $dx$  is the spacing between the receivers. The temporal frequency is simply the inverse of time ( $\frac{1}{t}$ ). The deghosting operator is again the inverse of the ghost operator multiplied by its complex conjugate and some added stabilization factor in the denominator ( $\frac{G^*}{GG^* + \lambda}$ ).

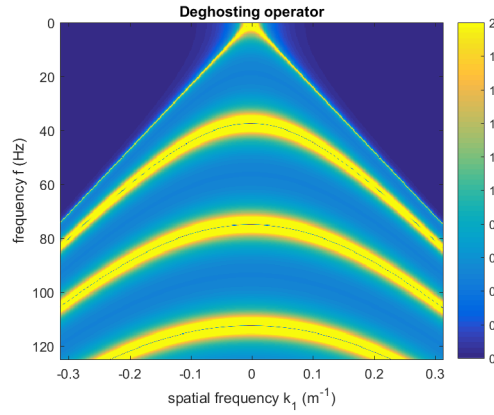


**Figure A-8:** Frequency spectrum of 2-D deghosting operator.

Figure A-8 illustrates the working of the inverse filtering technique in 2-D. It is similar to the 1-D case where the deghosting operator has full effect (high amplitude) in regaining the lost frequencies near the notches. If one looks really close at the middle of each notch there is a tiny area that indicates a low amplitude. In the case of vertical incidence ( $k=0 \text{ m}^{-1}$ ) the behavior is similar to the 1-D ghost operator (figure A-3) that indicates the shortcomings of the technique; the notches are not fully recovered. Another issue that might puzzle the reader is the downward bent shape of the ghost notches. At the notch frequencies (0,40,80,120,... Hz) and a spatial frequency/horizontal wavenumber ( $k_1$ ) of  $0 \text{ m}^{-1}$  the notches are flat. If the spatial frequency increases or decreases and the frequency increases, the ghost pattern bends away downward. This bending away downward can be explained by noting that if the spatial frequency is increased or decreased, the ghost notch will occur at a higher frequency. This is due to the fact that the propagation velocity in the water remains the same and the increase in frequency has to compensate for the increase in wavenumber, according to  $c = \frac{2\pi f}{k}$ . Figure A-9 displays the  $f - k$  spectra and  $t - x$  plots of a simple 2-D deghosting process. The figures on the left show the  $f - k$  spectra of the primary + ghost (top LHS) and deghosted result (bottom LHS). The deghosted result is similar to the 1D result (fig. A-5), where the frequencies are recovered except at the sharp notches. A small fraction of the notches has

not been filled for the same reason as for the 1-D case; the deghosting operator is a periodic function that will become zero at recurring frequencies (0,40,80,120,...,∞ Hz).

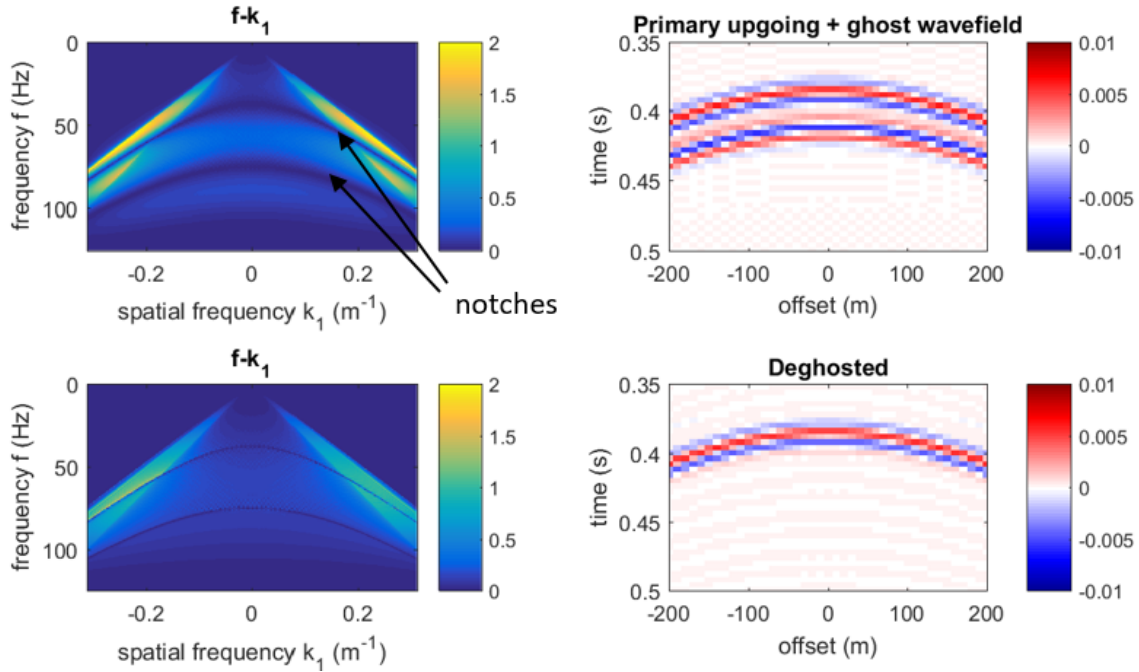


**Figure A-9:** 2D deterministic deghosting result. Left column indicates  $f - k$  spectra of data with ghost (top LHS) and deghosted (bottom LHS). Right column indicates zoomed in  $t - x$  plots of data with ghost (top RHS) and deghosted (bottom RHS).

The final result of the deghosting process should ideally result in the primary upgoing wavefield which is indicated in figure A-10.

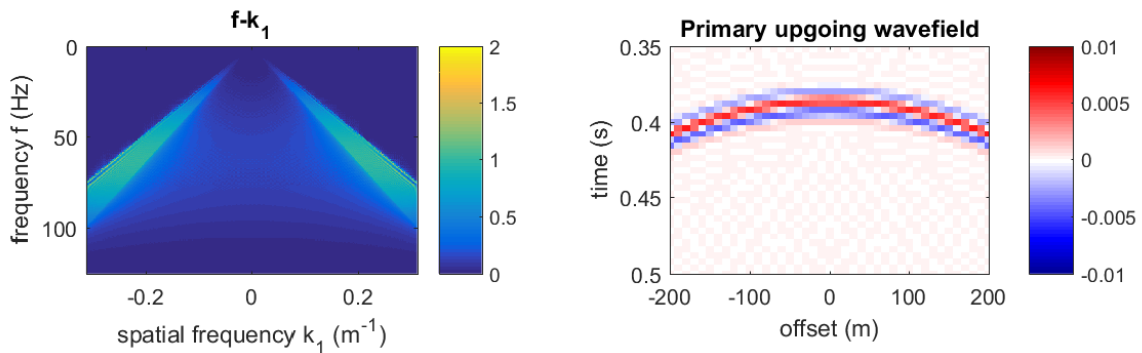


**Figure A-10:** The  $f - k$  spectra (LHS) and  $t - x$  plot (RHS) of 2D primary upgoing wavefield.

Changing the stabilization factor from 0.01 to 0.1 will give the same result as the 1D case; an increase of ringing artifacts will occur (fig. A-11). Note also that the notches are not filled up as much as the notches in the case  $\lambda = 0.01$  (bottom LHS figure A-9).

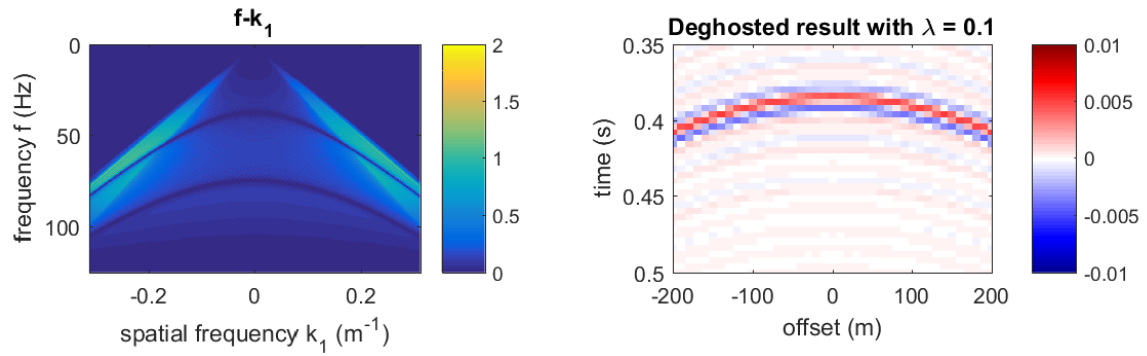
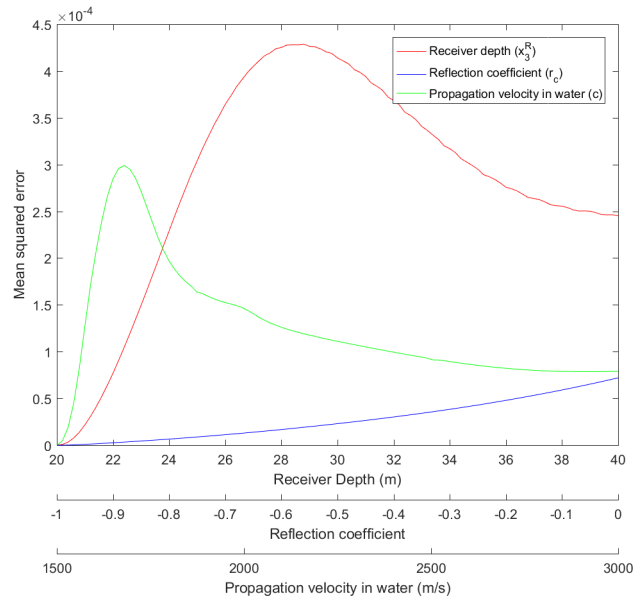


Figure A-11: 2D deghosted result with  $\lambda = 0.1$ .

Figure A-12 displays the sensitivity in the t-x domain for a different range of parameters. The tested parameters are:

Parameter	Correct value	Estimated values
$x_3^R$ (m)	20	20, 20.2, 20.4, ..., 39.8, 40
$r_c$	-1	-1, -0.99, -0.98, ..., -0.01, 0
$c$ (m/s)	1500	1500, 1515, 1530, ..., 2985, 3000

Table A-1: Different range of values of receiver depth, reflection coefficient and velocity used to compare with model.



**Figure A-12:** Sensitivity result when varying deghosting parameters, t-x domain.

The results are similar to the sensitivity analysis presented in chapter 2. A variation of the propagation velocity of seismic waves in water causes the greatest disturbance in the deghosting result, whereas the water surface reflectivity the least disturbance. The receiver depth causes the greatest change in the deghosting result after an increase of 20% of the original value.